A&A 671, A112 (2023)
https://doi.org/10.1051/0004-6361/202245657
© The Authors 2023

Astronomy & Astrophysics

GRB minimum variability timescale with Insight-HXMT and *Swift*

Implications for progenitor models, dissipation physics, and GRB classifications*

A. E. Camisasca[1], C. Guidorzi[1,2,3], L. Amati[3], F. Frontera[1,3], X. Y. Song[4], S. Xiao[4,5], S. L. Xiong[4], S. N. Zhang[4,5], R. Margutti[6,7], S. Kobayashi[8], C. G. Mundell[9], M. Y. Ge[4], A. Gomboc[10], S. M. Jia[4], N. Jordana-Mitjans[9], C. K. Li[4], X. B. Li[4], R. Maccary[1], M. Shrestha[11], W. C. Xue[4], and S. Zhang[4]

[1] Department of Physics and Earth Science, University of Ferrara, Via Saragat 1, 44122 Ferrara, Italy
e-mail: annaelisa.camisasca@unife.it
[2] INFN – Sezione di Ferrara, Via Saragat 1, 44122 Ferrara, Italy
[3] INAF – Osservatorio di Astrofisica e Scienza dello Spazio di Bologna, Via Piero Gobetti 101, 40129 Bologna, Italy
[4] Key Laboratory of Particle Astrophysics, Institute of High Energy Physics, Chinese Academy of Sciences, 19B Yuquan Road, Beijing 100049, PR China
[5] University of Chinese Academy of Sciences, Chinese Academy of Sciences, Beijing 100049, PR China
[6] Department of Astronomy, University of California, 501 Campbell Hall, Berkeley, CA 94720, USA
[7] Department of Physics, University of California, 366 Physics North MC 7300, Berkeley, CA 94720, USA
[8] Astrophysics Research Institute, Liverpool John Moores University, IC2, Liverpool Science Park, 146 Brownlow Hill, Liverpool L3 5RF, UK
[9] Department of Physics, University of Bath, Claverton Down, Bath BA2 7AY, UK
[10] Center for Astrophysics and Cosmology, University of Nova Gorica, Vipavska 13, 5000 Nova Gorica, Slovenia
[11] Steward Observatory, University of Arizona, 933 North Cherry Avenue, Tucson, AZ 85721-0065, USA

Received 9 December 2022 / Accepted 2 January 2023

ABSTRACT

Context. There has been significant technological and scientific progress in our ability to detect, monitor, and model the physics of γ-ray bursts (GRBs) over the 50 years since their first discovery. However, the dissipation process thought to be responsible for their defining prompt emission is still unknown. Recent efforts have focused on investigating how the ultrarelativistic jet of the GRB propagates through the progenitor's stellar envelope for different initial composition shapes, jet structures, magnetisation, and, consequently, possible energy dissipation processes. Study of the temporal variability – in particular the shortest duration of an independent emission episode within a GRB – may provide a unique way to distinguish the imprint of the inner engine activity from geometry and propagation related effects. The advent of new high-energy detectors with exquisite time resolution now makes this possible.

Aims. We aim to characterise the minimum variability timescale (MVT) defined as the shortest duration of individual pulses that shape a light curve for a sample of GRBs in the keV–MeV energy range and test correlations with other key observables such as the peak luminosity, the Lorentz factor, and the jet opening angle. We compare these correlations with predictions from recent numerical simulations for a relativistic structured – possibly wobbling – jet and assess the value of temporal variability studies as probes of prompt-emission dissipation physics.

Methods. We used the peak detection algorithm MEPSA to identify the shortest pulse within a GRB time history and preliminarily calibrated MEPSA to estimate the full width at half maximum duration. We then applied this framework to two sets of GRBs: *Swift* GRBs (from 2005 to July 2022) and Insight Hard Modulation X-ray Telescope (Insight-HXMT) GRBs (from June 2017 to July 2021, including the exceptional 221009A). We then selected 401 GRBs with measured redshift to test for correlations.

Results. We confirm that, on average, short GRBs have significantly shorter MVTs than long GRBs. The MVT distribution of short GRBs with extended emission such as 060614 and 211211A is compatible only with that of short GRBs. This is important because it provides a new clue concerning the progenitor's nature. The MVT for long GRBs with measured redshift anti-correlates with peak luminosity; our analysis includes careful evaluation of selection effects. We confirm the anti-correlation with the Lorentz factor and find a correlation with the jet opening angle as estimated from the afterglow light curve, along with an inverse correlation with the number of pulses.

Conclusions. The MVT can identify the emerging putative new class of long GRBs that are suggested to be produced by compact binary mergers. For otherwise typical long GRBs, the different correlations between MVT and peak luminosity, Lorentz factor, jet opening angle, and number of pulses can be explained within the context of structured, possibly wobbling, weakly magnetised relativistic jets.

Key words. radiation mechanisms: non-thermal – relativistic processes – gamma-ray burst: general – stars: jets

* Full Tables 1, 2, and 5 are only available at the CDS via anonymous ftp to cdsarc.cds.unistra.fr (130.79.128.5) or via https://cdsarc.cds.unistra.fr/viz-bin/cat/J/A+A/671/A112

Open Access article, published by EDP Sciences, under the terms of the Creative Commons Attribution License (https://creativecommons.org/licenses/by/4.0), which permits unrestricted use, distribution, and reproduction in any medium, provided the original work is properly cited.
This article is published in open access under the Subscribe to Open model. Subscribe to A&A to support open access publication.

1. Introduction

The prompt emission of γ-ray bursts (GRBs) is the first energetic and short-lived electromagnetic messenger produced by a relativistic jet that forms in at least two classes of progenitors: (i) binary compact object mergers, where at least one of the two components is thought to be a neutron star (NS; Eichler et al. 1989; Paczynski 1991; Narayan et al. 1992); and (ii) collapsars, massive stars whose core collapses into a compact object, which powers a relativistic jet that breaks out of the stellar envelope (Woosley 1993; Paczyński 1998; MacFadyen & Woosley 1999). Most GRBs of the former (latter) class have a typical duration of a few 0.1 s (> several seconds) and are therefore referred to as 'short' ('long'), hereafter SGRBs (LGRBs). The discovery of so-called soft extended emission short GRBs (hereafter SEE-SGRBs; Norris & Bonnell 2006), that is, GRBs whose duration is formally long ($T_{90} > 2$ s, usually taken as the boundary), but whose profile includes an initial hard subsecond spike followed by a several-second-long-lived soft tail, and for which evidence points to class (i), emphasised that duration alone can occasionally be misleading (e.g. Amati 2021). The occurrence of baffling SEE-SGRBs, such as 060614 (Gehrels et al. 2006; Della Valle et al. 2006; Fynbo et al. 2006; Jin et al. 2015) and the recent 211211A (Rastinejad et al. 2022; Gompertz et al. 2023; Yang et al. 2022; Troja et al. 2022; Xiao et al. 2022), shows that events of class (i) may exhibit time profiles that further challenge and elude this picture. Opposite cases of apparent SGRBs that instead belong to class (ii) have also been identified (Ahumada et al. 2021; Zhang et al. 2021; Rossi et al. 2022), so in hindsight the emerging picture raises the issue of a contamination between the two classes that is potentially more widespread than believed so far, purely based on time profiles. Consequently, to avoid confusion and adopting previous suggestions (Zhang 2006; Zhang et al. 2007; Kann et al. 2011; Tsvetkova et al. 2017), when talking about the progenitor case, hereafter we refer to (i) and (ii) candidates as Type-I and Type-II, respectively.

Many open and intertwined issues still enshroud the GRB prompt emission, including the question of which source of energy turns into γ-rays between bulk kinetic or magnetic. One may also seek to determine by which dissipation process they are ruled, the composition of the relativistic jet, and at what distance from the inner progenitor the dissipation takes place.

Among the distinctive properties are the variety and complexity of GRB light curves (LCs), which manifest as a wide range of variability over several timescales. While this complexity likely retains a wealth of information, a full understanding has yet to be found. This variability can be the result of several different contributions: (a) inner engine activity both in terms of short timescales and number of peaks (Kobayashi et al. 1997); (b) propagation of the relativistic flow through the stellar envelope, which in turn also depends on (c) the jet composition (Gottlieb et al. 2019, 2020a,b, 2021a,b); (d) geometry: structure of the jet and angle of the observer, $\theta_{\rm obs}$, with respect to the opening angle of the jet core, $\theta_{\rm j}$ (e.g. Salafia et al. 2016); and (e) a possible precessing or wobbling jet (Portegies Zwart et al. 1999; Portegies Zwart & Totani 2001; Fargion 2001; Reynoso et al. 2006; Lei et al. 2007; Budai et al. 2020), as suggested by state-of-the-art, 3D, general-relativity-magnetohydrodynamic (GRMHD) simulations (Gottlieb et al. 2022a.

Numerous definitions of GRB variability have been put forward in the literature, aimed at quantifying the net variance of the GRB signal once the contribution of the noise due to counting statistics (hereafter statistical noise) is removed. This was done either by summing the contributions of all timescales after excluding some kind of trend (e.g. Reichart et al. 2001; Fenimore & Ramirez-Ruiz 2000) or decomposing the signal variance over a timescale base. In the latter case, the decomposition can be done either in time (Li 2001; Margutti 2009; Margutti et al. 2011) or frequency domain, based on either Fourier analysis (Guidorzi et al. 2016; Dichiara et al. 2016) or wavelets (Golkhou & Butler 2014, hereafter GB14; Golkhou et al. 2015; Vianello et al. 2018). In spite of the scatter, variability was found to correlate with peak luminosity for LGRBs (Fenimore & Ramirez-Ruiz 2000; Reichart et al. 2001; Guidorzi et al. 2005), although the slope can vary remarkably depending on the definition of variability and other aspects (Guidorzi et al. 2006).

A related way to characterise the variability is the identification of the minimum variability timescale (MVT)[1], which is the shortest timescale on which uncorrelated power is found to be in significant excess of the statistical noise as well as of the correlated signal due to the overall temporal shape of the GRB LC. In principle this quantity helps to constrain the emitting region size and the activity of the inner engine and could help identify the different contributions (a)–(e) listed above, especially when it is studied in conjunction with other key properties.

The two classes of SGRBs and LGRBs have partially overlapping, but different, MVT distributions, with median rest-frame values of 10 and 45 ms, respectively, and very few (<10%) with ms MVT (Golkhou et al. 2015; see also MacLachlan et al. 2013). The MVT of LGRBs was found to correlate with the bulk Lorentz factor Γ_0 (Sonbas et al. 2015) estimated from the early afterglow peak, whenever this is due to the deceleration of the relativistic jet in the thin shell regime (Sari & Piran 1999; Molinari et al. 2007).

A drawback of most definitions lies in the meaning itself and how this is to be interpreted: while connections are sometimes found with simple properties, such as the individual pulse rise time (MacLachlan et al. 2012), the interpretation is not straightforward. This is partly due to the complexity of the GRB signal, which is short-lived, highly non-stationary, and occasionally has an evolving power density spectrum (e.g. Margutti et al. 2008). A common feature of most definitions of MVT is that the identification of one or more temporal structures associated with MVT relies on their relative weight in the total net variance of the GRB LC. As a consequence, a given spike could be identified or not, depending on its impact on the time-averaged power density spectrum.

In this paper, we adopted an alternative approach that builds on a simple definition of MVT as the full width at half maximum (FWHM) of the shortest (statistically significant) peak (hereafter $\rm FWHM_{min}$). The identification of statistically significant peaks is done using the sensitive and well-calibrated algorithm MEPSA (Guidorzi 2015). A similar idea, based on the identification of individual pulses within a GRB, was already proposed in the past (Bhat et al. 2012; Bhat 2013), but it was not explored any further. This approach has three main advantages: (1) the interpretation is straightforward; (2) it is related directly to a specific temporal structure within the overall GRB time profile and, as such, the probability of it being identified does not depend on its relative weight within the total variance of the GRB; and (3) a careful evaluation of how the measure of MVT is affected by the signal-to-noise ratio (S/N) is feasible and, consequently, of the impact on the correlations involving MVT. To this aim, we

[1] Shortened to "MTS" in some papers.

Table 1. First 10 GRBs of *Swift* sample.

GRB name	$\mathrm{FWHM_{min}}$ (s)	T_{90} (s)	z	N_{peaks}	Type
050117	$0.810^{+0.280}_{-0.208}$	166.648 ± 2.423	–	15	L
050124	$1.009^{+0.349}_{-0.259}$	3.936 ± 2.012	–	2	L
050126	$9.063^{+3.134}_{-2.329}$	48.000 ± 22.627	1.290	1	L
050128	$0.296^{+0.102}_{-0.076}$	28.000 ± 9.055	–	7	L
050202	$\leq 0.103^{+0.036}_{-0.026}$	0.112 ± 0.031	–	1	S
050215A	$6.238^{+2.158}_{-1.603}$	66.412 ± 5.307	–	1	L
050215B	$4.384^{+1.516}_{-1.127}$	11.044 ± 3.931	–	1	L
050219A	$7.432^{+2.570}_{-1.910}$	23.812 ± 2.258	0.211	1	L
050219B	$0.770^{+0.266}_{-0.198}$	28.720 ± 7.120	–	4	L
050223	$23.518^{+8.134}_{-6.044}$	22.680 ± 4.481	0.592	1	L

Notes. This table is available in its entirety in machine-readable form at the CDS.

carried out our analysis using two GRB catalogues with complementary energy passbands: the first GRB catalogue (Song et al. 2022) of the Insight Hard X-ray Modulation Telescope (Insight-HXMT; Li 2007; Zhang et al. 2020) and that of the Burst Alert Telescope (BAT, 15−150 keV; Barthelmy et al. 2005) aboard the *Neil Gehrels Swift* Observatory (Gehrels et al. 2004).

The HXMT, named 'Insight' after launch on June 15, 2017, is the first Chinese X-ray astronomy satellite. Its scientific payload consists of three main instruments: the Low Energy X-ray telescope (LE; 1−15 keV; Chen et al. 2020), the Medium Energy X-ray telescope (ME; 5−30 keV; Cao et al. 2020), and the High Energy X-ray telescope (HE; Liu et al. 2020). The HE consists of 18 NaI/CsI detectors which cover the 20−250 keV energy band for pointing observations. In addition, it can be used as an open sky GRB monitor in the 0.2−3 MeV energy range. The unique combination of a large geometric area (~5100 $\mathrm{cm^2}$) and of continuous event tagging with timing accuracy <10 µs, makes HXMT/HE an ideal instrument to study MVTs with GRBs. In this work, we investigated this possibility by carrying out a systematic analysis of the data acquired with HE, which was used as an open sky γ-ray monitor.

Section 2 describes the GRB samples; the data analysis is reported in Sect. 3, whereas results are in Sect. 4. We discuss the implications in Sect. 5 and conclude in Sect. 6. Hereafter, we assume the latest *Planck* cosmological parameters: $H_0 = 67.74\,\mathrm{km\,s^{-1}\,Mpc^{-1}}$, $\Omega_\mathrm{m} = 0.315$, $\Omega_\Lambda = 0.685$ (Planck Collaboration VI 2020).

2. Data set

2.1. *Swift*/BAT sample

We considered all GRBs detected by *Swift*/BAT in burst mode from January 2005 to July 2022. We extracted the mask-weighted LCs in the 15−150 keV energy band following the standard procedure recommended by the BAT team[2] with a set of different uniform bin times: 1, 4, 64, and 1000 ms. We excluded all the GRBs whose LCs were not entirely covered in burst mode. We then systematically applied MEPSA to each of the LCs. For each GRB, the $\mathrm{FWHM_{min}}$ was determined through the procedure described in Sect. 3. Finally, we ignored the GRBs for which either the $\mathrm{FWHM_{min}}$ or T_{90} is not significant. The final sample of GRBs includes 1291 GRBs (*Swift* sample hereafter). For 21 GRBs only an upper limit on the $\mathrm{FWHM_{min}}$ was derived. We also considered the duration of each GRB (expressed in terms of T_{90}) using the values by Lien et al. (2016), which cover up to October 2015. For the remaining GRBs we adopted the values reported by the BAT team through dedicated BAT refined Gamma-ray Coordinates Network (GCN) circulars[3]. For about one third of the sample (401/1291) the redshift is known.

Although a lower threshold was suggested for *Swift* (Bromberg et al. 2013), we take the value of 2 s as an approximate boundary between S- and LGRBs, in line with the traditional division (Kouveliotou et al. 1993) and with the choice of *Swift* team members (D'Avanzo et al. 2014). In this way, we obtained 78 SGRBs. In addition, the sample includes 24 SEE-GRBs[4]. The overall sample consists of 102 Type-I GRBs, that is 8% of the whole sample. Table 1 reports the data.

2.2. *Insight-HXMT/HE sample*

We considered all GRBs detected by Insight-HXMT/HE from June 2017 to June 2021, as catalogued by the Insight-HXMT team (Song et al. 2022). Since HE continuously acquires data in event mode, it has no trigger logic on board. For each GRB, whenever the GRB was detected in common by other experiments, such as *Swift*/BAT or *Fermi*/GBM, we took the trigger time provided by them as the GRB start. Differently, we determined the start time by visual inspection of the HE LC.

For each GRB, we extracted the event files and auxiliary files including time-resolved information about the detectors' dead time, spacecraft's attitude, and the position, within a time window from −300 to 300 s around the GRB time. Using the HE

[2] https://swift.gsfc.nasa.gov/analysis/threads/bat_threads.html

[3] https://gcn.gsfc.nasa.gov/gcn3_archive.html

[4] They are: 050724, 051227, 060614, 061006, 061210, 070714B, 071227, 080503, 090510, 090531B, 090715A, 090916, 110402A, 111121A, 150424A, 160410A, 161129A, 170728B, 180618A, 180805B, 181123B, 200219A, 211211A, 211227A.

units as an open-sky monitor, for each of the 18 HE detectors, we extracted a set of LCs with the same bin times as for the *Swift* sample (i.e. 1, 4, 64, and 1000 ms) selecting only the CsI events, as was done in Song et al. (2022). The LCs include dead-time corrected counts within the total energy passband from all 18 HE detectors summed together. The total energy passband depends on the HE operation mode:

- normal mode: 80−800 keV;
- GRB mode (low gain): 200−3000 keV.

We analysed 21 GRBs[5] separately; due to their very intense peak count rates, the onboard electronics of at least one physical data acquisition unit (PDAU; see Liu et al. 2020 for details) were temporarily unable to keep up with the exceptional rate of events to be recorded (see Xiao et al. 2020; Song et al. 2022 for details). We restricted our analysis to the time windows where no PDAU was saturated. For these GRBs, we consequently ended up with upper limits on the $\mathrm{FWHM_{min}}$. In the following, we consider the LCs summed over the 18 detectors.

The background was estimated in two independent ways: (i) through interpolation with a maximum of a third-degree polynomial within two time windows, preceding and following the GRB, respectively (the size of each time window varies for different GRBs and had to be determined by visual inspection); and (ii) by iterative interpolation of a unique time interval that includes both time windows used in (i) as well as the GRB interval. At every iteration, all the time bins whose counts exceeded the interpolated signal (where σ is the corresponding Poisson uncertainty) by $\geq 2\sigma$ are rejected. Iterations stop when no further bins are rejected. This iterative procedure was applied to the 1-s LC, and the resulting background model was then properly renormalised to the LCs with different bin times. To determine which of the two outcomes is to be used for each GRB, we calculated the null hypothesis probability (NHP) associated with a two-tail χ^2 test applied to the residuals of each LC with respect to each background model and chose the more probable one, provided that NHP was ≥1%.

With the exception of the saturated GRBs, we used the T_{90} values reported for the GRBs belonging to golden and silver samples of the HXMT GRB catalogue (Song et al. 2022). For the saturated sample, we used the T_{90} as reported on Konus-Wind, *Fermi*-GBM, and Insight-HXMT GCN circulars. If different estimates of T_{90} were provided by different experiments for a given GRB, we conservatively used a mean and an error that include all the values.

We decided to include the recent, exceptionally bright 221009A (Dichiara et al. 2022). Since it repeatedly saturated the electronics of Insight-HXMT/HE (Ge et al. 2022), we provided an upper limit on the $\mathrm{FWHM_{min}}$ as for the other saturated GRBs. We estimated T_{90} using the data of BepiColombo-MGNS in the 280−460 keV passband, which has one of the few unsaturated and publicly available time profiles (Kozyrev et al. 2022). The 2-s time resolution is too coarse to constrain the MVT, but it is enough for the T_{90}, given the very long duration. The background was interpolated linearly using the intervals $-900\,\mathrm{s} \leq t \leq 100\,\mathrm{s}$ and $670\,\mathrm{s} \leq t \leq 1600\,\mathrm{s}$, with t measured since 13:15:26.90 UTC.

[5] They are 171011B, 180113B, 180113C, 180218A, 180720B, 180914B, 181222B, 190103A, 190114C, 190305A, 190411A, 190415A, 190530A, 190606A, 190706C, 190928A, 191025B, 191227B, 201016A, 201227A, and 221009A. 200415A saturated the electronics too, but it was not considered as it is probably an extragalactic magnetar giant flare; (Yang et al. 2020; Fermi-LAT Collaboration 2021; Roberts et al. 2021; Svinkin et al. 2021).

Finally, we systematically ran MEPSA on all the LCs and applied the procedure described in Sect. 3 to determine the $\mathrm{FWHM_{min}}$ of each GRB as we did for the *Swift* sample (Sect. 2.1). Unlike for the BAT LCs, for which the Gaussian-noise regime is ensured by the fact that the rates are linear combinations of several thousands of independent detectors, in the case of the 1-ms LCs summed over all the 18 HE detectors the mean counts per bin amount to ≲10. Hence, the Gaussian-noise assumption is only approximately matched. To partially account for this deviation and use a more conservative estimate of the variance of a Poisson variate for small numbers, we corrected the uncertainties following the prescriptions by Gehrels (1986).

We ignored the GRBs with non-significant values for either $\mathrm{FWHM_{min}}$ or T_{90}, as we did with the *Swift* sample. The final sample of Insight-HXMT/HE includes 212 GRBs, 25 of which were detected in GRB mode, while the remaining ones in normal mode. Hereafter we will refer to them as the HXMT sample. For 14 GRBs, only an upper limit on the $\mathrm{FWHM_{min}}$ was obtained. Taking the value of 2 s as an approximate boundary between SGRBs and LGRBs, we find that 24 are SGRBs, while two are SEE-GRBs. Thus, 26 are Type-I GRBs, which corresponds to 12% of the total. This result shows that Insight-HXMT is more effective in detecting short hard GRBs than *Swift* (7%; Sect. 2.1).

For six GRBs, the redshift is known. There are 44 GRBs that were detected by *Swift*/BAT and Insight-HXMT and for which a comparative analysis of our results is feasible and done in Sect. 4.2. Data are reported in Table 2.

3. Data analysis

We applied MEPSA to the dataset described in Sect. 2 in order to obtain the $\mathrm{FWHM_{min}}$. In particular, for each GRB, we started from the 64-ms LC. A detected peak is considered a candidate when it satisfies the following two conditions: (i) $S/N > S/N_{\mathrm{min}}^{(\Delta t)}$, where the threshold depends on the LC bin time Δt; (ii) $\Delta t_{\mathrm{det}} > \Delta t_{\mathrm{det,min}}^{(\Delta t)}$, where Δt_{det} is the so-called detection timescale, a MEPSA parameter which defines the bin timescale that optimises the peak identification (Guidorzi 2015). Both sets of thresholds are reported in Table 3. Requirement (ii) is to ensure that the bin time is short enough to resolve the temporal structure: the duration of the peak must be greater than the size of the bin. This is the reason for setting the threshold to twice the corresponding bin time: $\Delta t_{\mathrm{det,min}}^{(\Delta t)} = 2\Delta t$. The different threshold values on the S/N for different Δt were calculated to keep the number of expected statistical fluctuations being classified as genuine peaks approximately constant: the shorter Δt and the correspondingly larger number of bins to be screened that span a given time interval.

We decided to start with $\Delta t = 64$ ms and systematically avoided research with finer resolutions because preliminary attempts showed that the number of peak candidates was higher than expected, especially in the HXMT data. The reason behind this behaviour is the presence of sub-millisecond spikes caused by the electronics repeatedly counting the large signal deposited by energetic cosmic rays (Wu et al. 2022). Whenever only (i) is fulfilled, we move to a finer time resolution (i.e. 4 ms and then 1 ms if necessary) and look for the same peak until both (i) and (ii) are satisfied; if (i) and (ii) are never satisfied, an upper limit on the $\mathrm{FWHM_{min}}$ is taken from the finest timescale for which (i) is satisfied. When no peak is found at 64 ms that fulfils both (i) and (ii), we move to the $\Delta t = 1$ s. If no qualified peak is found, the GRB is discarded because of poor S/N. Figure 1 shows a schematic description of the procedure. The

Table 2. First 10 GRBs of Insight-HXMT sample.

GRB name	$\mathrm{FWHM_{min}}$ (s)	T_{90} (s)	z	N_{peaks}	Type
170626A	$0.097^{+0.033}_{-0.025}$	12.690 ± 0.081	–	4	L
170626B	$1.969^{+0.681}_{-0.506}$	6.511 ± 1.120	–	2	L
170705A	$0.784^{+0.271}_{-0.201}$	18.460 ± 6.340	2.010	1	L
170708A	$0.041^{+0.014}_{-0.011}$	0.200 ± 0.022	–	1	S
170712A	$1.188^{+0.411}_{-0.305}$	8.511 ± 1.119	–	1	L
170718A	$6.802^{+2.353}_{-1.748}$	24.160 ± 3.322	–	1	L
170726A	$0.149^{+0.051}_{-0.038}$	22.871 ± 0.901	–	8	L
170728B	$\leq 0.275^{+0.095}_{-0.071}$	16.860 ± 2.371	–	2	L
170801A	$0.021^{+0.007}_{-0.005}$	0.460 ± 0.750	–	1	S
170802A	$0.033^{+0.012}_{-0.009}$	0.820 ± 0.014	–	2	S

Notes. This table is available in its entirety in machine-readable form at the CDS.

Table 3. Thresholds on S/N and on Δt_{det} corresponding to the different bin times that were adopted to determine the $\mathrm{FWHM_{min}}$.

Bin time Δt (ms)	$S/N_{\mathrm{min}}^{(\Delta t)}$	$\Delta t_{\mathrm{det,min}}^{(\Delta t)}$ (ms)
1	7.0	2
4	6.8	8
64	6.4	128
1000	6.0	2000

FWHM of each peak is estimated through the calibrated relation based on the combination of S/N and Δt_{det} (see Appendix A for details).

4. Results

4.1. Comparison between $\mathrm{FWHM_{min}}$ and other minimum variability timescale metrics

Our choice of adopting the $\mathrm{FWHM_{min}}$ as an indicator of the MVT of a given GRB LC in principle represents a different definition than other ones that appeared in the literature. In particular, the most distinctive feature of $\mathrm{FWHM_{min}}$ is that the duration of a possible, statistically significant, narrow pulse can be enough to qualify it as the MVT, irrespective of its impact on the overall variance of the GRB profile and for its physical impact. Nevertheless, it is worth exploring how the $\mathrm{FWHM_{min}}$ correlates with other metrics. To this aim, we selected a common sample of 467 BAT GRBs, for which GB14 estimated the MVT. Both GB14's and our estimates are derived from the same BAT data. Figure 2 shows the comparison between the $\mathrm{FWHM_{min}}$ and the corresponding MVT estimated by GB14, with equality shown by a solid line. The two metrics evidently correlate over four decades, with some scatter around equality: this result proves that, although strongly correlated, the two metrics are not completely interchangeable, with a sizeable fraction of cases for which they differ by up to one decade.

4.2. $\mathrm{FWHM_{min}}$ as a function of energy

Figure 3 shows the comparison of the $\mathrm{FWHM_{min}}$ as measured with both Insight-HXMT and *Swift*/BAT using the common sample of 44 GRBs, three of which only have an upper limit on the $\mathrm{FWHM_{min}}$ available. The distribution of the logarithm of the ratio between the two measures is approximately normal, with the mean value and standard deviation corresponding to a multiplicative factor of 2 and 3, respectively. Hence, the $\mathrm{FWHM_{min}}$ as measured with *Swift* is on average twice as long as that measured with Insight-HXMT. This is similar to the result obtained by Golkhou et al. (2015) from the comparison between *Fermi*/GBM and *Swift*/BAT, as one should expect due to the narrowing of pulses with energy.

Additionally, we can constrain the power-law index α of the relation $FWHM(E) \propto E^{-\alpha}$, where E is the geometric mean of the boundaries of the energy passband. To this aim, for each GRB in the common sample we did not restrict to the shortest pulse of each GRB, instead we calculated α considering the FWHM of the different peaks as detected with MEPSA in both HXMT and BAT data. The identification of the same peak, as seen in the two LCs, is assessed through the temporal coincidence within uncertainties. We identified 93 peaks, four of which were in SGRBs. For the energy values, we used the geometric mean of the boundaries of the corresponding energy bands (15−150 keV for BAT, 80−800 keV for HXMT normal mode, 200−3000 keV for HXMT GRB or low-gain mode; HXMT energy bands refer to the deposited energies of incident photons). We find $\alpha_{\mathrm{mean}} = 0.45 \pm 0.08$, $\alpha_{\mathrm{median}} = 0.54 \pm 0.07$, $\sigma = 0.77$; this result is consistent with the values derived modelling the autocorrelation function width (Fenimore et al. 1995): $\alpha = 0.37$ to 0.43 (see also Borgonovo et al. 2007, who found median values in the range from 0.21 to 0.29). Figure 4 displays the α distribution for all GRBs (black histogram), SGRBs (blue histogram), and LGRBs (red histogram).

4.3. $\mathrm{FWHM_{min}}$ versus T_{90}

Figure 5 shows the scatter plots of the $\mathrm{FWHM_{min}}$ and T_{90} for *Swift*/BAT and Insight-HXMT samples along with the corresponding marginal distributions. $\mathrm{FWHM_{min}}$ spans the range

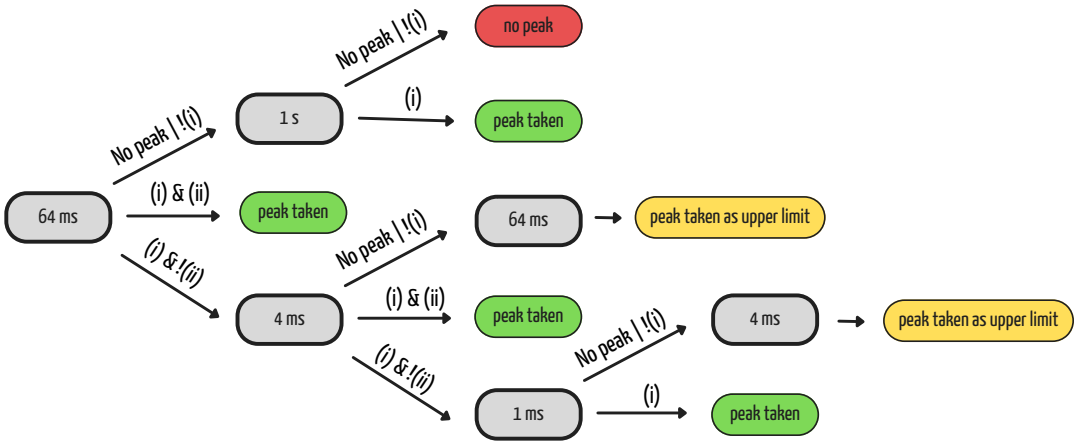

Fig. 1. A schematic description of the procedure adopted to determine the $\mathrm{FWHM_{min}}$ of each GRB (see Sect. 3).

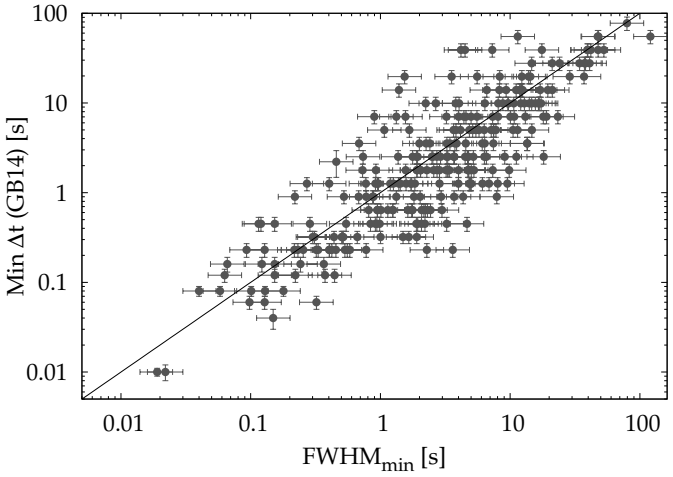

Fig. 2. Comparison between shortest FWHM as estimated with MEPSA (this work) and MVT estimated by GB14 for a common sample of *Swift*/BAT GRBs. Black line corresponds to equality.

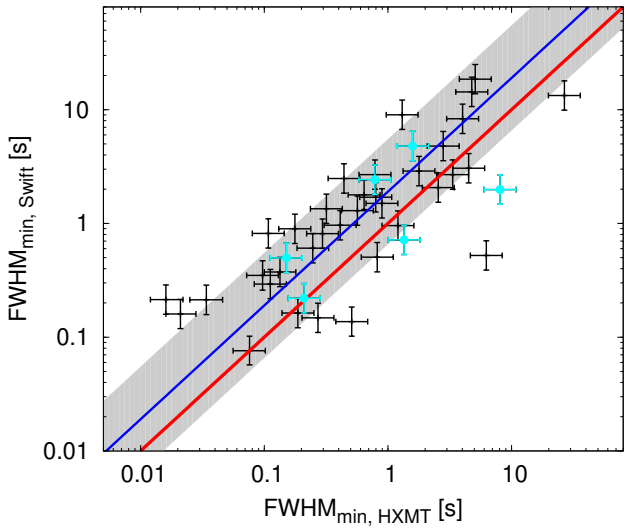

Fig. 3. FWHM as determined from Insight-HXMT/HE and *Swift*/BAT data for a sample of 44 GRBs in common. The red solid line shows the equality, while the blue line and the shaded area show the best proportionality relation and 1-σ region, corresponding to a factor of 2 and a relative scatter of a factor of 3, respectively. Cyan points are GRBs with spectroscopically measured redshift.

from 10^{-2} to 10^{2} s, whereas T_{90} spans from 10^{-2} to 10^{3} s (10^{2} s for Insight-HXMT). The bimodal nature of the marginal distribution of T_{90} seems to be slightly more evident in the Insight-HXMT sample, in spite of the lower number of GRBs. Equality is shown with a solid line. In addition, to guide the eye, we show lines that mark constant values for the ratio $r = T_{90}/\mathrm{FWHM_{min}}$: 10 (dashed), 100 (dash-dotted), and 1000 (dotted). Clearly, r increases with an increasing number of pulses within a GRB and/or with the presence of quiescent times. Most single-pulse GRBs lie in the region of $1 \lesssim r < 10$. Unsurprisingly, almost all SGRBs lie within this region. LGRBs instead span the $1 \leq r \lesssim 10^{3}$ range.

The marginal $\mathrm{FWHM_{min}}$ distributions of SGRBs and of LGRBs are evidently different: for the *Swift* sample, a Kolmogorov–Smirnov (KS) test[6] yields a 10^{-37} probability of being drawn from the same population; the logarithmic means of SGRBs and of LGRBs are, respectively, 0.2 and 4 s with a comparable scatter of 0.6 dex. Also in the Insight-HXMT sample, the two classes of S- and LGRBs have significantly different $\mathrm{FWHM_{min}}$ distributions, with a 3×10^{-12} probability of being drawn from a common population. The logarithmic mean values are 0.1 and 1.3 s for the S- and LGRBs with the same scatter of ∼0.6 dex, respectively, that is shorter than the corresponding quantities obtained in the softer energy band of the *Swift* sample, in line with the results of Sect. 4.2.

In the *Swift* sample we highlight the population of SEE-GRBs (green), with emphasis on two peculiar events whose LC and duration look like a typical LGRB one, but for which robust evidence for a compact binary merger progenitor rather than a collapsar was found: 060614 (Gehrels et al. 2006; Della Valle et al. 2006; Fynbo et al. 2006; Jin et al. 2015) and 211211A (Rastinejad et al. 2022; Gompertz et al. 2023; Yang et al. 2022; Troja et al. 2022). In spite of being just 24, their $\mathrm{FWHM_{min}}$ values are more similar to those of SGRBs than of LGRBs. While both KS and Anderson-Darling (AD)[7] tests between the $\mathrm{FWHM_{min}}$ of SGRBs and SEE-GRBs do not reject the common population null hypothesis, the comparison between LGRBs and SEE-GRBs does so with a 3.4×10^{-14} KS-

[6] The two-sample KS test was done using `scipy.stats.ks_2samp`.

[7] The two-sample AD test was done using `scipy.stats.anderson_ksamp`.

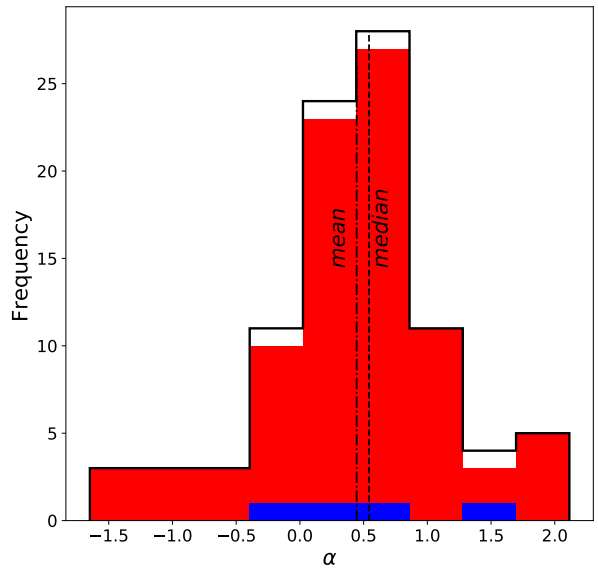

Fig. 4. Distribution of power-law index α ($FWHM \propto E^{-\alpha}$) for all the peaks that were identified in the GRB data of both *Swift* and HXMT (black histogram): SGRBs (filled blue histogram) and LGRBs (filled red histogram). Dash-dotted and dashed lines represent the mean (0.45± 0.08) and the median (0.54 ± 0.07) values, respectively.

probability (AD probability $<10^{-3}$). Therefore, the $\mathrm{FWHM_{min}}$ is a promising metric to identify SEE-GRBs, even when the LC does not look like a single spike followed by a long, soft, and smooth tail, but rather shows multiple peaks extending over several seconds, as was the case of 060614 and 211211A. This suggests that the contamination of long GRBs with a $\mathrm{FWHM_{min}} \lesssim 0.1$ s that are currently misclassified as Type-II GRBs could be higher than expected, as was recently put forward from the observations of events like 211211A.

As a further check, we also show 18 LGRBs for which the collapsar origin is not disputable, thanks to the identification of an associated SN (gold points)[8]. Although a few of them have a $\mathrm{FWHM_{min}}$ that is comparable with that of SEE-GRBs, the bulk of SN-associated GRBs have longer MVTs, more representatively of the entire population of Type-II GRBs. Furthermore, the comparison between LGRBs associated with SN and SEE-GRBs done with KS and AD tests rejects the common population null hypothesis with a probability of 1.2×10^{-5} ($<10^{-3}$) for KS (AD).

To the Insight-HXMT plot (see Fig. 5, right panel), we added the saturated GRBs (cyan), highlighting the cases of 190114C and 221009A; for 5[9] of the 21 saturated GRBs it was not possible to find any eligible peak. These GRBs are SGRBs, and the time windows that are not saturated are too short for estimating $\mathrm{FWHM_{min}}$.

4.4. Dependence of $\mathrm{FWHM_{min}}$ and T_{90} on redshift

For the BAT sample with measured redshift, we studied whether the T_{90} and $\mathrm{FWHM_{min}}$ distributions show evidence for cosmological time dilation. We calculated the geometric mean of groups of GRBs: 30 (6) GRBs each for LGRBs (SGRBs) and then fitted the geometric mean values as a function of $(1+z)^{\alpha}$, with the power-law index α free to vary. Figure 6 shows the results, which suggest that there is no evidence of a dependence on redshift (α being compatible with zero), at least as far LGRBs are concerned. The reason is that the different effects at play combine in such a way that the cosmological dilation is not dominant, as also found by previous investigations (Kocevski & Petrosian 2013; GB14; Golkhou et al. 2015; Littlejohns & Butler 2014). In particular, there are two main effects that contribute to mask the impact of cosmic dilation: (a) for a given observer energy passband, further GRBs are observed in a rest-frame harder band, which implies narrower temporal structures, according to the narrowing of pulses with energy (Norris et al. 1996; Fenimore et al. 1995); (b) the S/N of a LC decreases with increasing z so that only the brightest portion of the LC can be detected (Kocevski & Petrosian 2013).

For SGRBs the results seem to indicate values of both $\mathrm{FWHM_{min}}$ and T_{90} increasing with redshift. The reason for this apparently different behaviour from LGRBs is not obvious; in particular, it is not clear why the same effects mentioned above for LGRBs do not appear to affect SGRBs in a comparable way. It is nonetheless worth noting that each SGRB group includes just six events, a choice forced by the small number of SGRBs with known z, so our accuracy in estimating the standard deviation of $\mathrm{FWHM_{min}}$ and T_{90} for SGRB groups is lower than for LGRBs. In any case, the redshift range is shorter than that of LGRBs, so in principle the cosmic dilation correction does not have the same impact as it should for LGRBs, notwithstanding that there are counteracting effects at play. Moreover, should we correct the $\mathrm{FWHM_{min}}$ values for the SGRB sample, the result of statistically different distributions of $\mathrm{FWHM_{min}}$ for LGRBs and SGRBs would be reinforced. For this reason, we conservatively avoided correcting the observer-frame value for $\mathrm{FWHM_{min}}$ for cosmological time dilation.

4.5. Peak rate versus $\mathrm{FWHM_{min}}$

The peak rate $\mathrm{PR_{max}}$ is defined as the peak rate of the most intense pulse of a given GRB. To explore the relation between isotropic-equivalent peak luminosity (L_{p}) and $\mathrm{FWHM_{min}}$, we first need to understand the relation between $\mathrm{PR_{max}}$ and $\mathrm{FWHM_{min}}$ focusing on the selection effects that inevitably come into play. We did not consider the cosmological time dilation in its simplest formulation, which is $\mathrm{FWHM_{min}}/(1+z)$, given the interplay of different effects already discussed in Sect. 4.4. $\mathrm{PR_{max}}$ appears to be anti-correlated with $\mathrm{FWHM_{min}}$ (Fig. 7). However, the selection effect at play here is to be evaluated carefully: for a very short pulse to be detected, its peak rate must be high enough to ensure the required minimum S/N. To this aim, we simulated a number of fast rise exponential decay (FRED) pulses covering the $\mathrm{PR_{max}}$ versus $\mathrm{FWHM_{min}}$ space of interest and counted the fraction of pulses that were identified by our procedure. As a result, we modelled the detection efficiency, ϵ_{det}, defined as the fraction of simulated pulses that are correctly identified, as a function of both $\mathrm{PR_{max}}$ and $\mathrm{FWHM_{min}}$: $\epsilon_{\mathrm{det}}(\mathrm{PR_{max}}, \mathrm{FWHM_{min}})$. We found that the dependence is approximately linear in the logarithms for both *Swift* and HXMT data sets:

$$\epsilon_{\mathrm{det}} = a \log_{10}\left(\frac{FWHM_{\mathrm{min}}}{\mathrm{s}}\right) + b \log_{10}\left(\frac{\mathrm{PR_{max}}}{\text{rate unit}}\right) + c, \quad (1)$$

where the rate units are either counts $\mathrm{s^{-1}\,det^{-1}}$ (*Swift*/BAT) or counts $\mathrm{s^{-1}}$ (HXMT/HE). For BAT, the best-fit parameters are

[8] They are: 060729, 090618, 091127, 100316D, 101219B, 111228A, 120422A, 120714B, 120729A, 130215A, 130427A, 130831A, 140506A, 161219B, 171205A, 180728A, 190114C, and 190829A.
[9] They are: 181222B, 190606A, 191025B, 191227B, and 201227A.

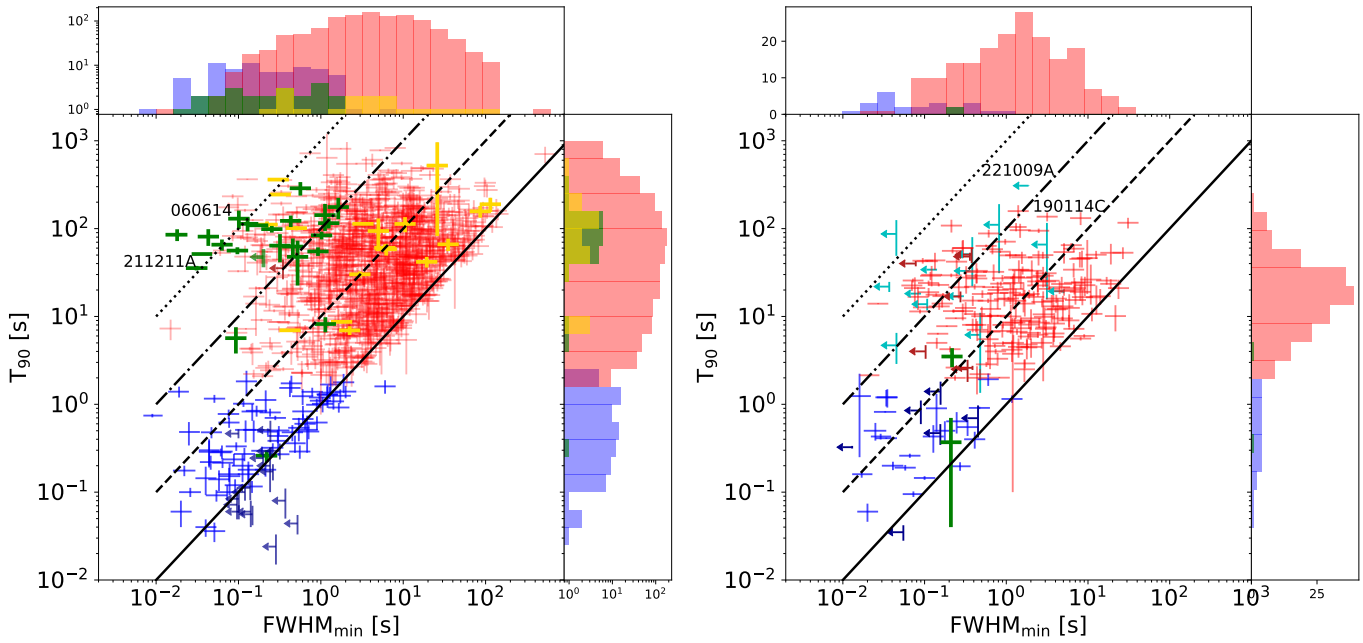

Fig. 5. Scatter plot of $\mathrm{FWHM_{min}}$ and T_{90} for the *Swift*/BAT sample (*left panel*) and for the Insight-HXMT sample (*right panel*) along with the corresponding marginal distributions for three distinct populations of SGRBs (blue), LGRBs (red), and SEE-GRBs (green). Gold points are LGRBs with an associated SN. We highlight two SEE-GRBs, 060614 and 211211A, for which there is strong evidence of a binary merger rather than a collapsar origin. Cyan points refer to the Insight-HXMT saturated GRBs. We highlight 190114C and 221009A because of their high extreme energy (MAGIC Collaboration 2019; Frederiks et al. 2022). We do not consider *Swift* data where $T_{90} < \sigma_{T_{90}}$. Solid, dashed, dash-dotted, and dotted lines represent the equality, 10^1, 10^2, and 10^3 factor, respectively.

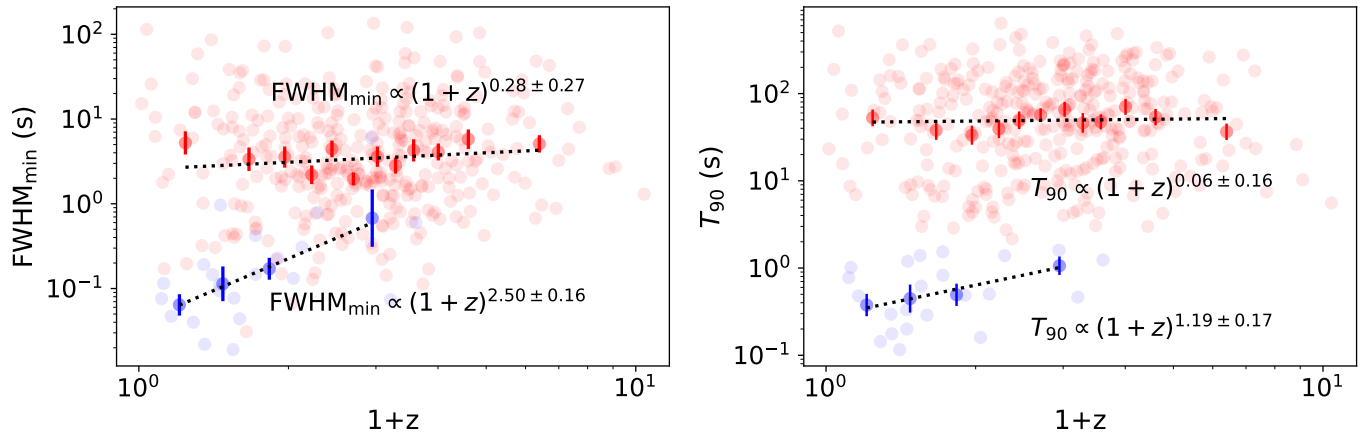

Fig. 6. $\mathrm{FWHM_{min}}$ versus $(1 + z)$ (*left panel*) and T_{90} versus $(1 + z)$ (*right panel*) for the *Swift* sample as seen in the observer frame. Red (blue) dots correspond to LGRBs (SGRBs). Lighter dots refer to individual GRBs; darker ones refer to T_{90} geometrical mean of groups of 30 (6) LGRBs (SGRBs), sorted with increasing z.

$a = 0.78$, $b = 1.42$, and $c = 1.64$, and it is clipped either to 0 for negative values, or to 1 for values exceeding it. One can conveniently invert Eq. (1) to express the minimum value for $\mathrm{PR_{max}}$ required for a pulse with a given $\mathrm{FWHM_{min}}$ to be detected, which in the case of *Swift*/BAT becomes

$$\mathrm{PR_{max}^{(BAT)}} \geq 0.35\ \mathrm{cts\,s^{-1}\,det^{-1}} \left(\frac{FWHM_{\mathrm{min}}}{\mathrm{s}}\right)^{-0.55} 10^{0.7\,(\epsilon-1)}. \quad (2)$$

Figure 7 shows the results for both data sets; *Swift*/BAT (left panel) and HXMT (right panel) are shown as a colour-coded shaded area with detection efficiency being split into ten different ranges, from 0 to 1. This selection effect clearly affects the observed correlation between the two quantities for both classes of SGRBs and LGRBs.

Replicating similar simulations and analysis for the HXMT sample, we obtained a similar result, which is described by Eq. (1) with the following parameters: $a = 1.78$, $b = 3.05$, and $c = -8.40$. The analogous condition of Eq. (2) for HXMT is therefore

$$\mathrm{PR_{max}^{(HXMT)}} \geq 1200\ \mathrm{cts\,s^{-1}} \left(\frac{FWHM_{\mathrm{min}}}{\mathrm{s}}\right)^{-0.58} 10^{0.33\,(\epsilon-1)}. \quad (3)$$

4.6. Peak luminosity versus $\mathrm{FWHM_{min}}$

When we move from the observer to the GRB rest frame by replacing $\mathrm{PR_{max}}$ with the intrinsic quantity L_{p}, the problem of accounting for this bias becomes more complicated, due to the wide range in luminosity distance D_{L} spanned by the subsample

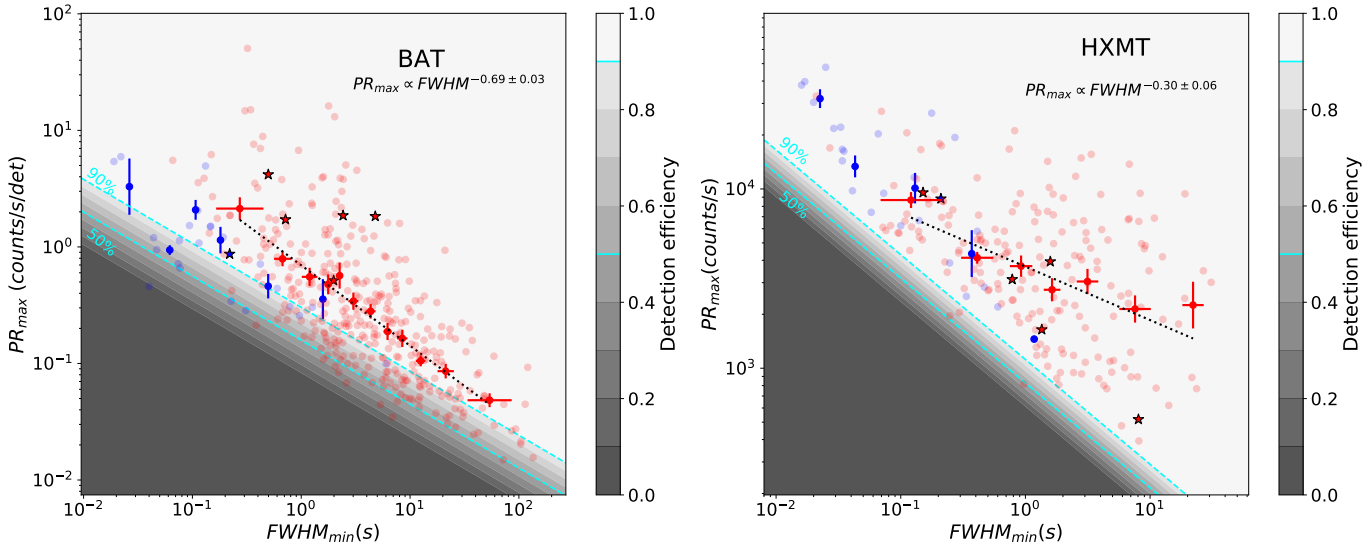

Fig. 7. Peak rate versus $\mathrm{FWHM_{min}}$ for the *Swift* (*left*) and HXMT (*right*) samples. Blue dots correspond to Type-I GRBs (i.e. SGRBs and SEE-GRBs), and red ones correspond to Type-II GRBs. Lighter dots refer to single GRB data, darker ones refer to geometrical mean of data of groups of GRBs sorted with increasing z. For Type-I, each group is composed 6 of GRBs; for Type-II, each group is composed of 30 GRBs. Stars refer to the six GRBs in common between the *Swift* sample and HXMT sample. Dotted lines indicate the best fit of Type-II GRBs. The shaded areas show ten different regions with detection efficiency spanning the 0−1 range. Cyan dashed lines show the 50% and 90% detection efficiency contours.

with measured redshift. In fact, a given peak rate corresponds to a range in luminosities which is dominated by the range spanned by D_L^2.

Given the paucity of GRBs with measured redshift in the HXMT sample, we only analysed L_p as a function of $\mathrm{FWHM_{min}}$ for the *Swift* sample with known z. We estimated L_p for this sample by renormalising the peak count rate by the ratio between total counts and the fluence (in units of erg cm^{-2} in the 15−150 keV energy band), as published by the BAT team[10]. This procedure assumes a time-averaged spectrum, which is equivalent to neglecting any spectral evolution. However, for our purposes, the impact of an error on L_p up to a factor of a few is negligible overall.

We split the sample into nine subsets, with luminosity distance evenly spaced logarithmically, and considered the impact of detection efficiency in the L_p–$\mathrm{FWHM_{min}}$ plane independently of each other. The results are shown in Fig. 8; the selection effect clearly affects the final correlation. In particular, two properties are evident: (i) the absence of relatively low luminosity GRBs with short $\mathrm{FWHM_{min}}$ (bottom left corner of each panel) is clearly an observational bias; (ii) the absence of luminous GRBs with a long $\mathrm{FWHM_{min}}$ (top right corner of each panel) is an intrinsic propriety of GRBs and suggests the possible existence of a maximum radiated energy within a single pulse (e.g. Dado & Dar 2022). To better appreciate this possibility, in each panel we show a grid with constant isotropic-equivalent released energy values of a single pulse, roughly estimated as $E_{iso}^{(pulse)} \approx L_p$ $\mathrm{FWHM_{min}}$.

Taken at face value, for the sample of BAT Type-I GRBs with measured z there is no evidence of correlation between L_p and $\mathrm{FWHM_{min}}$, possibly due to the relatively few GRBs. On the contrary, in the case of Type-II GRBs the two observables do correlate: null-hypothesis probabilities given by Pearson's linear-rank- (calculated on logarithmic values) and Spearman's and Kendall's rank-correlation tests are 1.5×10^{-21}, 2.6×10^{-23}, and 9.8×10^{-22}, respectively. However, the key aspect is understanding the extent by which this correlation is driven by the selection bias.

To this aim, we carried out a suite of simulations under the assumption that L_p is distributed independently of $\mathrm{FWHM_{min}}$ and hence no intrinsic correlation exists. For each of the nine subsets with different redshift bins we randomly generated as many points in the $\mathrm{FWHM_{min}}$–L_p plane as those in the true subset, taking the very same values of L_p and assuming, for the $\mathrm{FWHM_{min}}$, a Gaussian kernel density estimation[11] of the observed $\mathrm{FWHM_{min}}$ distribution of the entire LGRB sample with measured z as the probability density distribution. For each point to be accepted, we also set two conditions: (1) we randomly ran a Bernoulli trial assuming a probability given by the detection efficiency calculated at that point according to Eq. (1), and only the points with an outcome of 1 were taken; (2) L_p $\mathrm{FWHM_{min}} \leq E_{iso,max}^{(pulse)}$, i.e. we required that the isotropic-equivalent pulse energy did not overcome the highest value observed in the corresponding real subsample. Each subset trial continued until the number of accepted simulated points was equal to the real ones. The rationale behind point (1) is mimicking the effect of the selection bias, whereas the purpose of (2) is to account for the absence of a very luminous and long $\mathrm{FWHM_{min}}$ that is observed in the real sample. Every such round ended up with a simulated sample that shared the same number of Type-II GRBs as the real one and was affected by the same selection bias, with no intrinsic correlation between L_p and $\mathrm{FWHM_{min}}$. We simulated 10^4 such samples and derived a density map in the $\mathrm{FWHM_{min}}$–L_p plane to be compared with the real sample. Figure 9 shows the result. While the synthetic population does exhibit a correlation, as expected, it also appears more clustered than the real set.

To quantitatively assess how compatible the real and all the simulated samples are, we adopted the following approach: for each of them, we calculated the three correlation coefficients as we did for the real sample and obtained the corresponding distributions. Figure 10 shows the p-value distributions of the

[10] https://swift.gsfc.nasa.gov/archive/grb_table/

[11] We used the `scipy.stats.kde.gaussian_kde()` function.

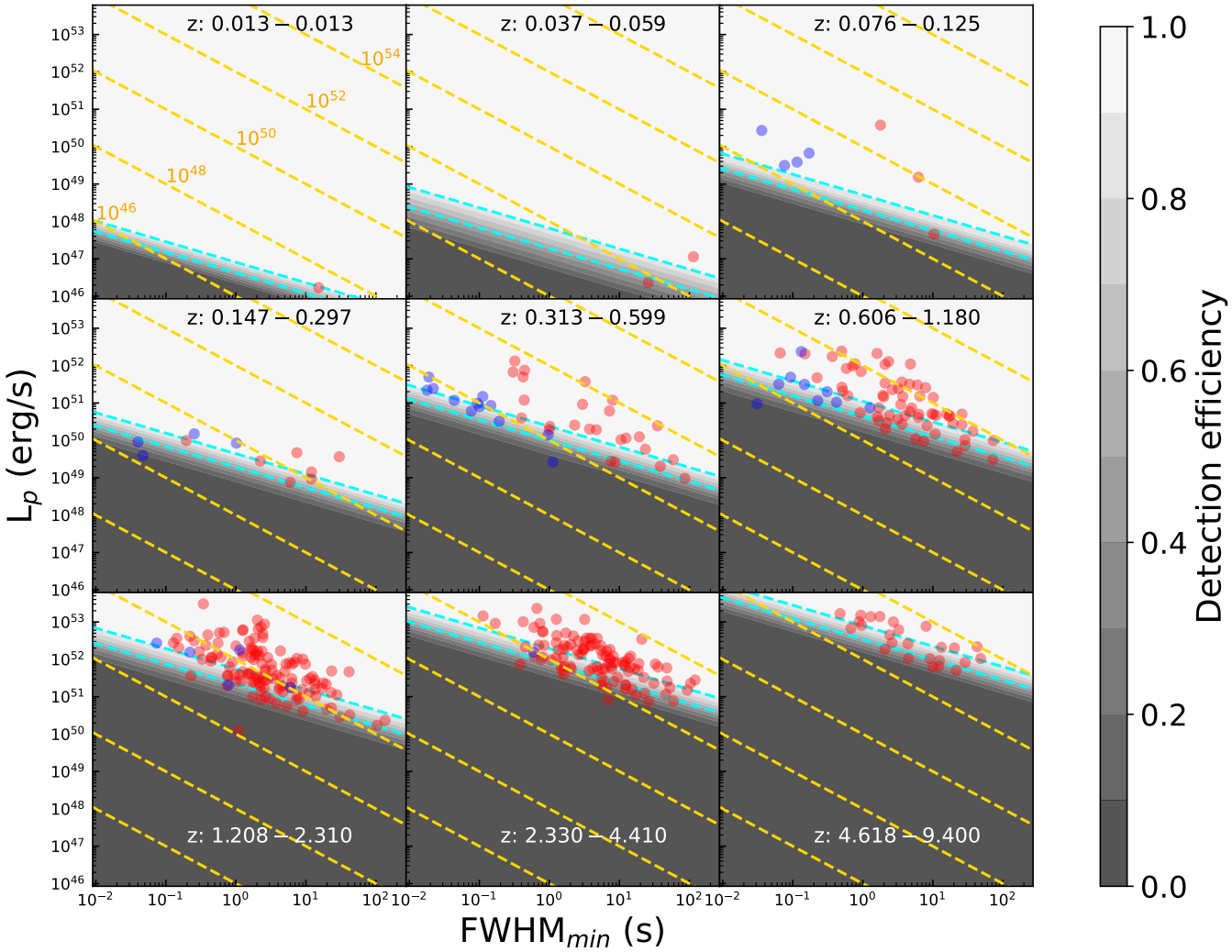

Fig. 8. Peak luminosity versus $\mathrm{FWHM_{min}}$ for the *Swift*/BAT sample split into nine redshift bins with constant logarithmic space in luminosity distance; blue dots correspond to Type-I GRBs, and red ones correspond to Type-II GRBs. Dashed cyan lines correspond to 90% and 50% detection efficiency (vertical bar). Gold dashed lines represent loci of constant isotropic-equivalent released energy (in erg) of each individual peak, approximately calculated as $E_{\rm iso} = L_{\rm p}\ \mathrm{FWHM_{min}}$.

simulated samples, compared with the analogous quantities obtained for the real sample. The real sample exhibits a more significant correlation than simulated samples do: for each of the three correlation tests, only ≤20 synthetic samples out of 10^4 exhibited lower p values than the real sample.

We further explored how tightly this result depends on the assumed distribution of $\mathrm{FWHM_{min}}$: in fact, the observed one is inevitably the result of the same selection bias, whose impact we aim to study. We then repeated the same suite of simulations by assuming broader $\mathrm{FWHM_{min}}$ distributions, in particular extending towards small values. As a result, the comparison between the simulated and the real correlation coefficients essentially did not change, so the conclusion that the observed correlation cannot be entirely ascribed to the selection bias still holds.

4.7. Number of peaks versus $\mathrm{FWHM_{min}}$

We investigated the role of the number of peaks within a GRB, as determined with MEPSA, in the $\mathrm{FWHM_{min}}$–$L_{\rm p}$ correlation. We therefore split the Type-II GRB sample with measured z into four groups with comparable size, depending on the number of peaks that was previously established with MEPSA: $N_{\rm peaks} = 1, 2, 3$ or 4, ≥5. The left panel of Fig. 11 shows the result. GRBs with the largest number of pulses evidently cluster in the most luminous and narrow $\mathrm{FWHM_{min}}$ region. To understand whether this is mainly due to a S/N effect, we selected the 1/3 with the narrowest pulse with the highest S/N (threshold of $S/N > 12.26$). The result is shown in the right panel of Fig. 11 and clearly proves that the conclusion remains unaffected. To further characterise the link between number of peaks and $\mathrm{FWHM_{min}}$, in Fig. 12 we show both observables in a scatter plot, where both colour and symbol size show the S/N. Notably, the $\mathrm{FWHM_{min}}$ significantly shifts towards lower values for GRBs with increasing numbers of pulses.

In principle, if the probability density function of the FWHM of a peak is the same for all GRBs, regardless of the number of peaks, a GRB with more peaks is more likely to have a small $\mathrm{FWHM_{min}}$, since more peaks means more trials. However, Fig. 12 (top panel) clearly rules this case out; in fact, this putative distribution should result from sampling the $N_{\rm peaks} = 1$ observation, which is clearly incompatible with the $\mathrm{FWHM_{min}}$ distribution of GRBs with several peaks. We confirmed this through

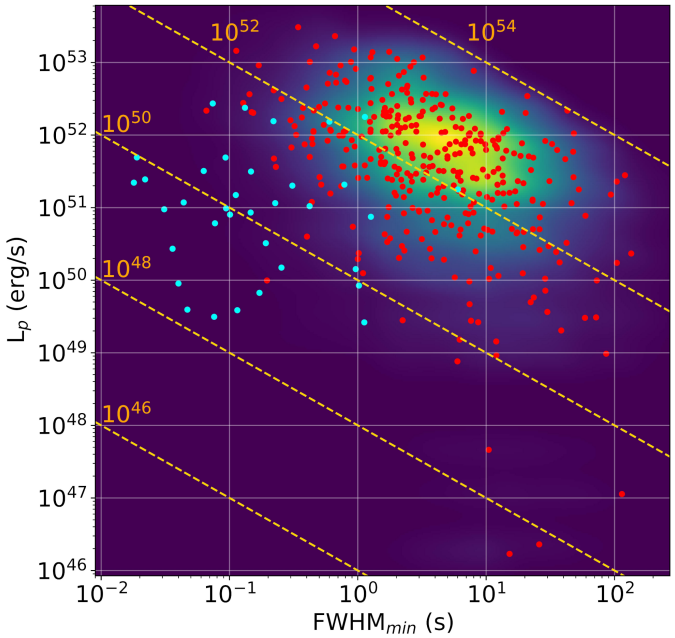

Fig. 9. Peak Luminosity L_p versus FWHM$_{min}$ for the *Swift*/BAT Type-II GRB sample (red circles). The colour-coded density map is the result of a simulated sample of Type-II GRBs that accounts for the selection effects shown in Fig. 8 under the assumption of no correlation between L_p and FWHM$_{min}$. For comparison, we also show SGRBs (cyan circles). Gold dashed lines represent loci with constant isotropic-equivalent released energy of each individual peak, approximately calculated as $E_{iso} = L_p$ FWHM$_{min}$.

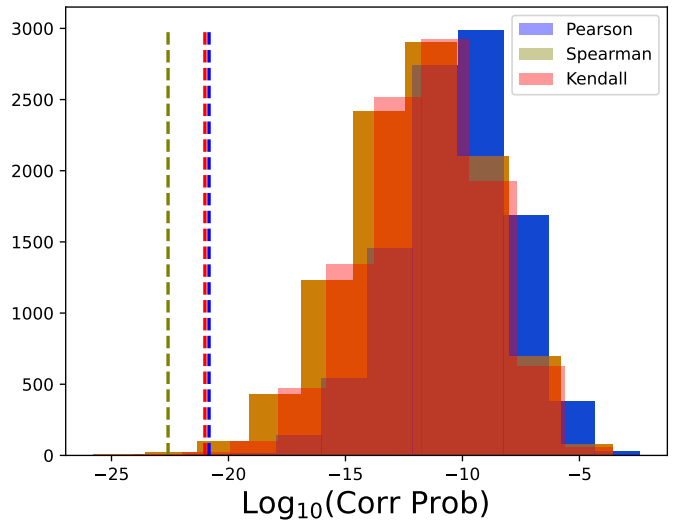

Fig. 10. FWHM$_{min}$–L_p correlation probability distributions of the simulated samples of Type-II GRBs, compared with the corresponding values obtained for the real sample of Type-II GRBs with measured z (vertical lines).

the following test: we considered all the *Swift* Type-II GRBs (regardless of the knowledge of z) with $N_{peaks} \geq 10$ (hereafter Obs10 sample). We then generated a population of fake GRBs (hereafter Sim10) with the same distribution of number of peaks as Obs10 (but with 100 times as many GRBs as Obs10), where each peak was chosen randomly from the distribution of GRBs with $N_{peaks} = 1$ (hereafter Obs1). We determined the FWHM$_{min}$ distribution of Sim10 and compared with that of Obs10 through two-population KS and AD tests. The probability that the two distributions of FWHM$_{min}$ are drawn from the same parent populations is 3×10^{-9} ($<10^{-3}$) with KS (AD) test. Using the same procedure with the HXMT sample, so including GRBs with unknown z (bottom panel of Fig. 12), we obtain a probability of 5×10^{-4} ($<10^{-3}$) according to the KS (AD) test.

4.8. Lorentz factor versus FWHM$_{min}$

To study the relation between MVT and Lorentz factor of the ejecta, we selected a subsample of Type-II GRBs for which an estimate of the latter was available in the literature. To this aim, we considered the following references: Lü et al. (2012), Yi et al. (2017), Xue et al. (2019), and Ghirlanda et al. (2018), along with a couple of additional references relative to individual GRBs: 111228A (Xin et al. 2016) and 150910A (Xie et al. 2020). All of these estimates, except for the GRBs of Xue et al. (2019), who obtained pseudo estimates based on the $E_{p,i}$–L_{iso}–Γ_0 relation (Liang et al. 2015), are based on the peak time of the early afterglow, interpreted as the deceleration of the fireball in the thin shell regime. Because of this, we assumed the Γ_0 values obtained from the deceleration peak for the GRBs in common. In any case, we graphically distinguish the different sources, to spot any possible difference. Our final sample consists of 131 GRBs, 39 of which have Γ_0 from the deceleration peak from Lü et al. (2012), Yi et al. (2017), Xin et al. (2016), and Xie et al. (2020), and 92 are pseudo values from Xue et al. (2019).

We treated the sample of Ghirlanda et al. (2018) separately, given that this is a rich collection that resulted from a homogeneous selection and treatment, and which also provides a set of lower limits on Γ_0 for many GRBs. Specifically, we calculated Γ_0 using their Eq. (11), taken from Nava et al. (2013). The estimated values were obtained for 50 GRBs that our sample shares with their golden and silver samples, while for the remaining 74 common GRBs we calculated the corresponding lower limits. We checked the mutual consistency of the estimated values taken from Ghirlanda et al. (2018) and the other references for a sample of common GRBs (41 values and 50 lower limits), and we found only a few incompatible estimates, whereas most estimates differ by $\lesssim$20%, and a dozen or so lower limits are incompatible with the estimates provided by the other works.

Figure 13 shows the results. The left panel shows the GRBs with colour-coded references for the Γ_0 estimates, whereas the right panel uses the sample in common with Ghirlanda et al. (2018). The anti-correlation is evident for both data sets, although significantly scattered.

It is not straightforward to understand the impact of the selection bias affecting the sample of FWHM$_{min}$ discussed in Sect. 4.6. Consequently, the apparent power-law slope of this correlation should be taken with care. Yet, interestingly, both data sets show an overall consistency with FWHM$_{min} \propto \Gamma_0^{-2}$, as shown by the dashed lines that correspond to constant values of $R = 2\,c\,\Gamma_0^2$ FWHM$_{min}$, which is the typical distance at which the dissipation of energy into γ-rays is supposed to take place. Almost all GRBs lie in the $10^{15} \lesssim R/\mathrm{cm} \lesssim 10^{17}$ range.

This range appears to be larger than 10^{13}–10^{14} cm, which is usually estimated in the case of internal shocks (e.g. Zhang & Mészáros 2004). However, there are several cases for which the estimates are consistent with our results: for a number of *Swift* GRBs for which the early X-ray afterglow steep decay could be interpreted as high-latitude emission, the onset time of this decay enabled to obtain $R \geq 10^{15}$–10^{16} cm (Lyutikov 2006; Kumar et al. 2007; Lazzati & Begelman 2006;

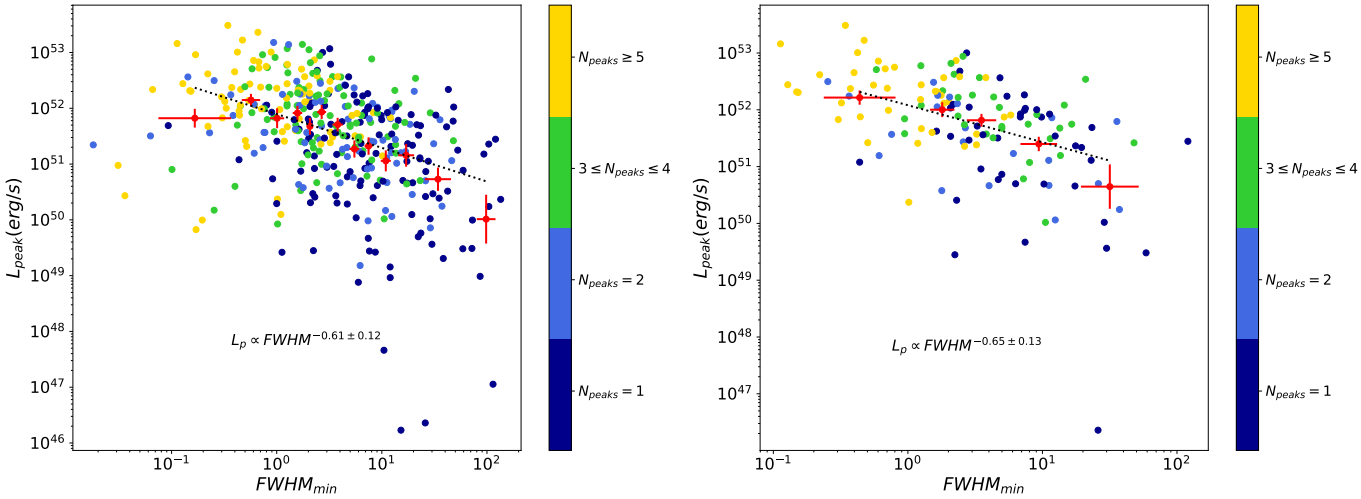

Fig. 11. Peak Luminosity versus $\mathrm{FWHM_{min}}$ for the *Swift* sample of Type-II GRBs for different number of peaks N_{peaks} (*left panel*); L_{p} versus $\mathrm{FWHM_{min}}$ for the *Swift* sample of Type-II GRBs, $S/N > 12.26$ (*right panel*), for different number of peaks N_{peaks}. Red dots refer to geometrical mean of groups of GRBs, with each group including 30 GRBs, independently of N_{peaks}.

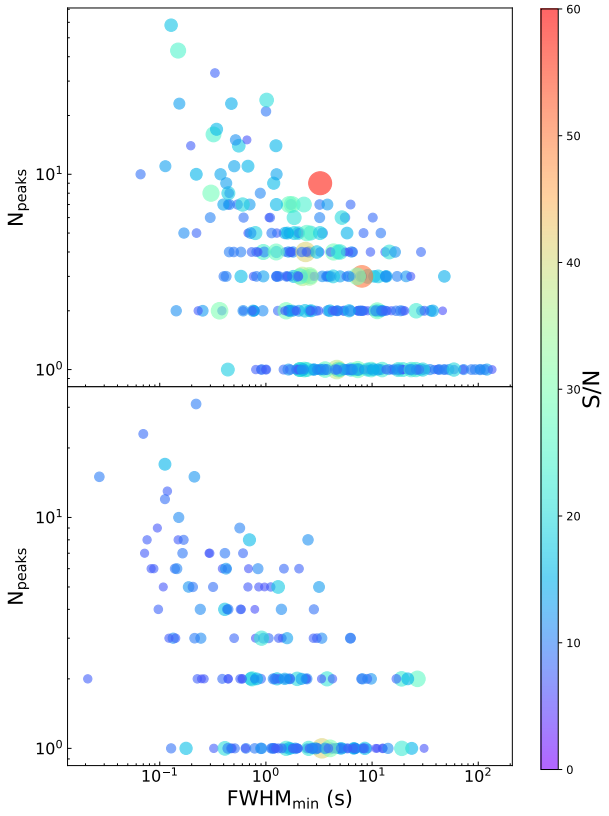

Fig. 12. Number of peaks versus $\mathrm{FWHM_{min}}$, Type-II GRBs for the *Swift* sample (*top panel*; here only GRBs with known z are shown for the sake of clarity) and HXMT sample (*bottom panel*). Symbol size and colour scale with S/N.

Hascoët et al. 2012). Also, for the naked-eye burst 080319B, $R \gtrsim 10^{16}$ cm was found, due to its bright prompt optical emission, which requires a synchrotron self-absorption frequency that is not too far above the optical band (Racusin et al. 2008; Kumar & Panaitescu 2008).

Different models can accommodate these values for R; for a Poynting flux-dominated outflow, a typical value of 3×10^{16} cm is predicted (Lyutikov & Blandford 2003). Alternatively, hybrid models such as the Internal Collision-induced MAgnetic Reconnection and Turbulence (ICMART; Zhang & Yan 2011) based on internal shocks, in which the dissipation mechanism is magnetic reconnection, also predict $R \sim 10^{15}$–10^{16} cm. Also, classical multi-zone internal shocks with reasonable Lorentz factor distributions for the wind of shells can predict dissipation radii in the range 10^{15}–10^{16} cm, whereas the possible associated high-energy (HE) neutrinos and ultra-high-energy cosmic rays (UHECRs) are mostly expected to be accelerated at distances ∼10–100 times closer to the engine (Bustamante et al. 2015, 2017). Our results may suggest that, if most GRB internal shocks take place above $\sim 10^{15}$ cm, that would explain why bright GRB prompt emission is not accompanied by HE neutrinos, at least as long as low-luminosity GRBs are ignored. This is in agreement with the upper limit of 1% on the contribution due to cosmological GRBs to the observed HE neutrino diffuse flux (Abbasi et al. 2022).

For each GRB we also compared the dissipation radius with the deceleration one, R_{dec}, at which the ejecta decelerates, which corresponds to the time at which the afterglow LC peaks. In particular, we took the Γ_0 and afterglow peak times of the sample by Ghirlanda et al. (2018) and verified that it was $R < R_{\mathrm{dec}}$ for all GRBs.

4.9. Jet opening angle versus $\mathrm{FWHM_{min}}$

We explored the relation between the MVT and jet opening angle, θ_{j}, as measured from the afterglow modelling for the GRBs for which evidence of an achromatic jet break was found. To this aim, we took the values reported in Zhao et al. (2020) in the two cases of ISM and wind environments. The resulting subset with measured θ_{j} includes 57 of our Type-II GRB sample with a measured $\mathrm{FWHM_{min}}$ and the number of peaks. Figure 14 shows the results for ISM (left panel) and wind (right panel); the information on the number of pulses is colour-coded.

Despite the apparent scattering, there is evidence of a correlation between jet opening angle and MVT with significance values of a few times 10^{-3} (Table 4). Motivated by the result in Fig. 14, we further tested the apparent clustering of GRBs with numerous peaks in the narrow jet–short MVT through a 2D,

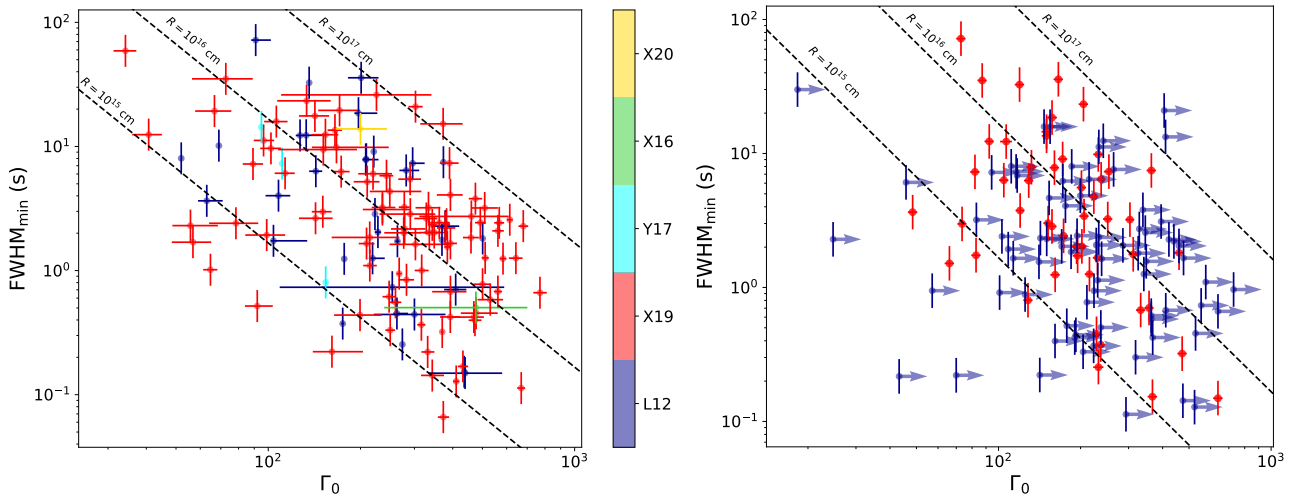

Fig. 13. FWHM$_{min}$ versus the initial Lorentz factor Γ_0 for a number of Type-II GRBs. *Left*: the values for the latter were taken from different data sets, which are colour-coded: L12 (Lü et al. 2012), X19 (Xue et al. 2019), Y17 (Yi et al. 2017), X16 (Xin et al. 2016), and X20 (Xie et al. 2020). Dashed lines correspond to the typical distance $R = 2\,c\,\Gamma_0^2\,\mathrm{FWHM}_{min}$ at which the dissipation process responsible for the prompt emission could take place. *Right*: same as left, except that we calculated Γ_0 from the data set by Ghirlanda et al. (2018). Red points are the GRBs belonging to their golden and silver samples, while blue points are lower limits on Γ_0.

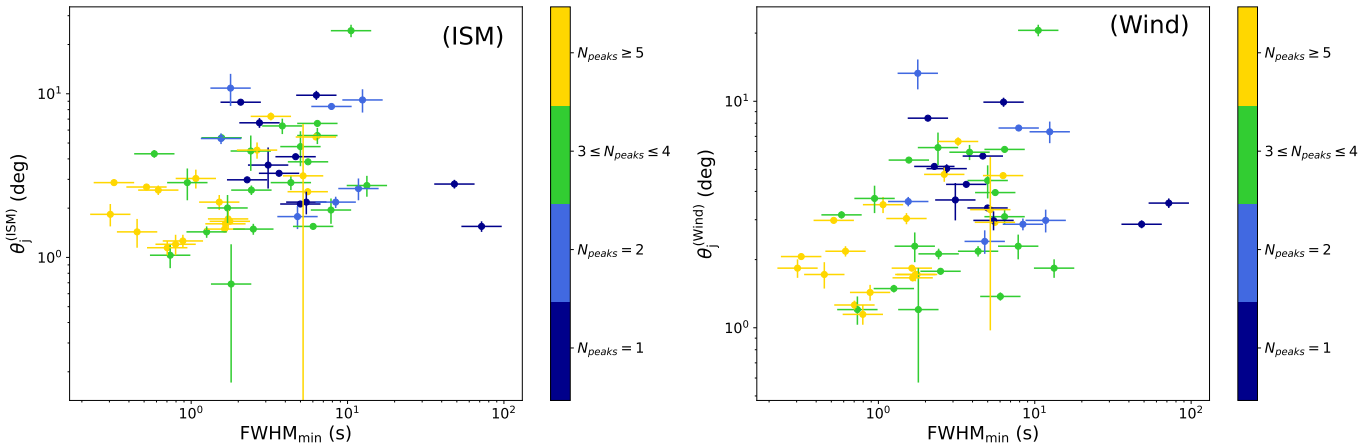

Fig. 14. Jet opening angles versus FWHM$_{min}$ for a set of Type-II GRBs for which both quantities could be estimated, assuming two different circumburst environments: ISM (*left*) and wind (*right*). Colours indicate the number of pulses.

Table 4. *P*-values of tests of correlation between MVT and jet opening angle for a sample of 57 Type-II GRBs displayed in Fig. 14.

Environment	Test	*p*-value
ISM	Pearson	2.4×10^{-2}
ISM	Spearman	5.6×10^{-3}
ISM	Kendall	5.2×10^{-3}
Wind	Pearson	4.6×10^{-3}
Wind	Spearman	2.0×10^{-3}
Wind	Kendall	4.4×10^{-3}

two-population KS test (Press et al. 1992) after dividing the sample into two groups, one including 18 GRBs with $N_{peaks} \leq 2$ and another including 39 GRBs with $N_{peaks} > 2$. Using the ISM (wind) values of θ_j, the probability that the number of peaks is uncorrelated with the position in the FWHM$_{min}$–θ_j plane is 4.1×10^{-3} (1.5×10^{-3}), equivalent to 2.9σ (3.2σ).

5. Discussion

Our results show that the observation of millisecond-long individual pulses is very rare in either class of GRBs. At one end, even if they exist, their identification is limited by instrumental sensitivity, given the strong dependence of the detection threshold on the FWHM$_{min}$ (Fig. 7). At the other end, we do observe rare GRBs with a peak rate high enough to ensure the possibility of detecting ms-long pulses, but in practice this rarely seems to be the case. The short end of the MVT distributions of both Type-I and Type-II GRBs extends to ∼10 ms within a factor of a few, depending on the energy passband. The two classes have overlapping MVT distributions, although the populations are statistically different. In this respect, SEE-GRBs, that is Type-I GRBs with an ambiguous time profile, exhibit an average MVT that is shorter than that of Type-II GRBs, making our MVT estimate a useful indicator of the progenitor class. In SEE-GRBs, whose environmental properties are indistinguishable from those of SGRBs (Fong et al. 2022; Nugent et al. 2022), the presence of a prolonged γ-ray activity characterised by a longer MVT that follows an initial spike could hint to

Table 5. First ten GRBs of *Swift* sample.

GRB name	L_p (10^{50} erg s^{-1})	Γ_0	Ref.	$\Gamma_0^{(G)}$	θ_j^{ISM} (rad)	θ_j^{Wind} (rad)
050126	4.13 ± 0.66	–	–	–	–	–
050219A	0.47 ± 0.04	–	–	–	–	–
050223	0.58 ± 0.08	–	–	–	–	–
050315	37.4 ± 3.0	–	–	–	0.111 ± 0.012	0.104 ± 0.008
050318	38 ± 4	–	–	57 ± 2	–	–
050319	95 ± 15	–	–	–	0.053 ± 0.007	0.061 ± 0.005
050401	912 ± 76	254^{+335}_{-145}	L12	554 ± 25	0.018 ± 0.003	0.021 ± 0.003
050416A	5.44 ± 0.85	–	–	101 ± 6	–	–
050505	311 ± 40	–	–	–	–	–
050525A	69.4 ± 1.5	268 ± 5	X19	224 ± 10	0.050 ± 0.011	0.065 ± 0.009

Notes. $\Gamma_0^{(G)}$ is the Lorentz factor from Ghirlanda et al. (2018) using Eq. (11) therein from Nava et al. (2013). This table is available in its entirety in machine-readable form at the CDS.

a long-lived, downward-spinning protomagnetar (Metzger et al. 2008; Bucciantini et al. 2012), a scenario that can also account for the complex broadband evolution exhibited by GRBs such as 180618A (Jordana-Mitjans et al. 2022). There are alternative interpretations, such as the one proposed to explain 211211A, in which the SEE would be produced by the prolonged accretion-powered activity of a newly formed black hole (BH), ruled by the strong magnetic field of one of the merging NSs (Gao et al. 2022). Regardless of the possible presence of the SEE and of its interpretation, the shorter MVT of Type-I GRBs appears to be a distinctive property with respect to the bulk of Type-II events. Although the nature of the inner engines that power the two classes could be similar (e.g. either a supramassive ms-magnetar or an hyperaccreting newly formed BH), the longer MVT in Type-II GRBs might be due to the engine variability being smeared out by the interaction with the massive envelope, whereas in Type-I the central engine variability imprint in the jet is retained throughout the propagation in less massive merger ejecta (e.g. see Gottlieb et al. 2022b). The other major difference between the two classes is the apparent absence of correlation between MVT and peak luminosity for Type-I GRBs, as shown in Fig. 9.

Concerning the properties of Type-II GRBs with measured redshifts, upon a careful evaluation of the involved selection effects on both luminosity and $\mathrm{FWHM}_{\mathrm{min}}$, we confirm that L_p and MVT do correlate, although a mathematical description that is corrected for the selection effects requires more extensive simulations that go beyond the scope of the present investigation. Additional information comes from the other correlations that we report here, and it involves MVT: in particular, (Type-II) GRBs that display many (>2) pulses have short MVTs on average (typically in the range of 0.01−1 s), are more luminous, have a higher bulk Lorentz factor, and, whenever the information is available, tend to have narrower jets or a smaller off-axis angle (see Table 5).

The jet opening angle θ_j is usually estimated from afterglow modelling and, in particular, from the observation of an achromatic break in the afterglow light curves that would correspond to the time at which the Lorentz factor Γ of the forward shock is such that $1/\Gamma \sim \theta_j$. While this is true for an on-axis observer, for $\theta_{obs} \neq 0$ but $\theta_{obs} < \theta_j$, the jet break time is actually set by the furthest edge from the observer, i.e. when the relativistic beaming decreases to the point at which $1/\Gamma \sim \theta_j + \theta_{obs}$ (van Eerten et al. 2010). In practice, when one also includes other factors, such as jet spreading, angular structure of a jet (as opposed to the simplistic case of a top-hat jet), radial fluid structure, and arrival time effects, deviations of the afterglow LC from simple power laws hinder an accurate measure of both jet and observer angles (van Eerten & MacFadyen 2012). Besides this, for increasing observer angles, but still $\theta_{obs} < \theta_j$, the jet break time may occur correspondingly later by a factor of 3−5 (De Colle et al. 2012). Consequently, the variable that we found to correlate with the MVT is likely more indicative of $(\theta_j + \theta_{obs})$ or, at least, of a combination of both θ_j and θ_{obs} rather than θ_j alone for an on-axis view ($\theta_{obs} \simeq 0$).

A simple interpretation of these correlations invokes a structured jet viewed through a range of different observer angles for different GRBs. Simulations suggest that the angular structure of a GRB jet consists of a flat core with an opening angle θ_j, followed by a power-law decline ($E_{iso} \propto \theta^{-\delta}$ for $\theta_j < \theta < \theta_c$) that models the so-called jet-cocoon interface (JCI). This is an interface layer between the jet core and the cocoon which extends to θ_c (Gottlieb et al. 2021a). The power-law index δ depends on the jet magnetisation: $\delta \sim 3$ for a weakly magnetised jet and $\delta \sim 1-2$ for a purely hydrodynamic jet. This difference arises from the different degree of mixing between jet and cocoon at the JCI, which in turn affects the baryon loading of jet: a magnetised jet, whose existence is also supported by early-time optical polarisation measurements (e.g. Gomboc et al. 2008; Mundell et al. 2013; Japelj et al. 2014; Steele et al. 2017), would suffer from a reduced mixing, with less energy transferred to the JCI and a consequent steeper energy angular profile (Gottlieb et al. 2020b).

Assuming similar values for θ_j for different GRBs as could be plausible in a quasi-universal jet structure (e.g. see Salafia et al. 2020 and references therein), or at least assuming that the spread of values of θ_{obs} is greater than that of θ_j for the observed population, the variety of values measured from the afterglow LC for the jet opening angle, which is actually more revealing of $(\theta_j + \theta_{obs})$, mostly reflects the range of θ_{obs}. For a relatively on-axis view, observed high Lorentz factor, high isotropic-equivalent peak luminosity are naturally accounted for. A short MVT and the abundance of pulses would suggest that we are looking through the jet core at the inner engine activity, unaffected by smoothing and blending that instead would characterise a more off-axis view, but still close to the JCI boundary ($\theta_{obs} \sim \theta_j$) because of lower Doppler boosting and longer arrival time delays (e.g. see Salafia et al. 2016). In addition, the LC blending could hinder the identification of distinct adjacent pulses, thus explaining why these GRBs show fewer pulses

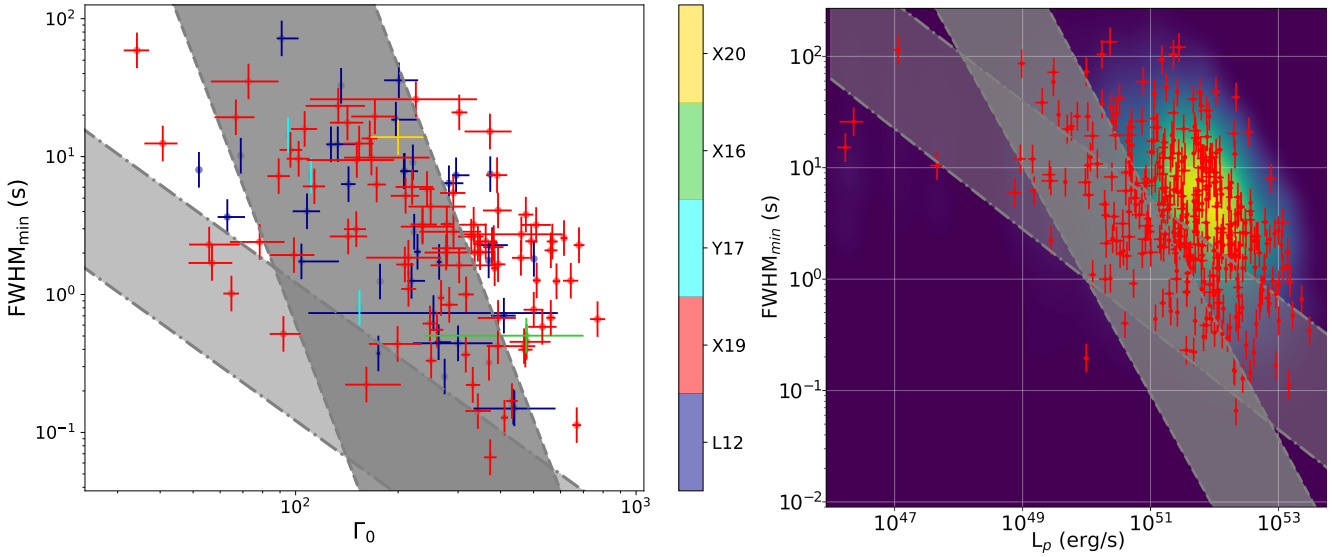

Fig. 15. FWHM$_{min}$ versus the initial Lorentz factor Γ_0 for a number of Type-II GRBs, with the predictions discussed by Xie et al. (2017), highlighted by the light shaded region between dash-dotted lines ($\nu\bar{\nu}$ annihilation mechanism) and by the dark shaded region between dashed lines (BZ mechanism). *Left*: same as Fig. 13. *Right*: same as Fig. 9, except that the two axes are swapped for ease of comparison with the expectations discussed by Xie et al. (2017).

on average. Concerning more off-axis GRBs, i.e. those with $\theta_j < \theta_{obs} < \theta_c$, they would appear as low-luminosity GRBs, which are mostly missing from present GRB catalogues.

A possible additional key property is suggested by recent 3D GRMHD simulations of the temporal evolution of a jet that results from a collapsar: some shocked gas would free-fall towards the newly formed BH and would be then deflected by the jet towards the accretion disc, which would consequently make the jet tilt randomly with respect to the BH rotational axis (Gottlieb et al. 2022c). The resulting jet would break out of the photosphere with a typical opening angle of $\theta_j \sim 6°$ and would wobble around with an angle of $\theta_t \sim 12°$ and a hybrid composition of magnetic and thermal energy due to the variable mixing. In this picture, the short MVT (0.01−0.1 s) would reflect the inner engine activity, possibly due to random fluctuations in the accretion process and launching mechanism, whereas long (1−10 s) interpulse times would occur whenever the jet points away from the observer (Gottlieb et al. 2022a). While the possibility of precessing jets in GRB sources is not new (Portegies Zwart et al. 1999; Portegies Zwart & Totani 2001; Fargion 2001; Reynoso et al. 2006; Lei et al. 2007), the stochastic nature of this wobbling, supported by state-of-the-art simulations, suggests that a multi-pulsed, luminous GRB with a short MVT and high Lorentz factor could be due to a jet wobbling around the line of sight, thus giving rising to more short pulses and, on average, exposing the variability of the inner engine during the frequent on-axis alignments. Less luminous GRBs, with fewer pulses and longer MVTs would harbour wobbling jets that are on average more misaligned with respect to the line of sight; these GRBs would correspond to the cases in which the angle between the time-average pointing direction of the jet and the line of sight is similar to the jet opening angle, $\langle\theta_{obs}\rangle \sim \theta_j$. This would turn into fewer pulses, given that the jet would spend more time with the line of sight off the jet core. The scatter of the observed correlations could be explained as being due to the fact that, even for such a GRB, the probability of a temporary fortuitous on-axis view, thus giving a narrow pulse, is not negligible, although less likely. This interpretation is supported by some Monte Carlo simulations of randomly wobbling structured jets: using a different definition of variability related to the number of pulses, a connection is predicted between variability and the jet opening angle as measured from the afterglow light curves (Budai et al. 2020), which agrees with our result.

A similar correlation between θ_j (or $\theta_j + \theta_{obs}$, as explained above) and a former definition of variability was already established by Kobayashi et al. (2002) for a few GRBs with measured quantities available at the time. According to their interpretation, GRBs with constant energy may result in different jet masses, so a smaller mass loading would be associated with a narrower jet, higher Lorentz factor, and isotropic-equivalent luminosity, as supported by simulations.

The scaling between the MVT versus Lorentz factor Γ_0 and the MVT versus luminosity may help constrain the mechanism used by the inner engine to power the relativistic jet. In this respect, Xie et al. (2017) considered two alternative scenarios that invoke a BH: (i) extraction of the BH rotational energy through the magnetic field sustained by the accretion disc according to the Blandford & Znajek mechanism (BZ; Blandford & Znajek 1977); (ii) a neutrino-dominated accretion flow (NDAF; Popham et al. 1999), whose neutrinos and antineutrinos annihilate and power the jet. In the BZ mechanism there is also an NDAF that supports and influences the magnetic field, which in turn suppresses the baryon loading from the neutrino-driven wind. In either case the MVT is determined by the viscous instability of the NDAF. In Fig. 15 we show our results on the correlations between the MVT and Γ_0 (left panel) and between the MVT and peak luminosity (right panel), along with the regions expected in each of the two scenarios: the light shaded region between dash-dotted lines refers to the $\nu\bar{\nu}$ annihilation mechanism, whereas the dark shaded region between dashed lines refers to the BZ one. The values of each set of model parameters are the same as the ones that are considered in Xie et al. (2017): as a consequence, while both regions can be shifted parallely, their slopes are more of a distinctive property of each and, as such, should be considered. While the slopes of the MVT–Γ_0 predicted relations seem to be overall compatible with

the data set, which is significantly scattered, the same comparison in the MVT–L_p plane seems to favour the BZ mechanism, as also argued by Xie et al. (2017). The $\nu\bar{\nu}$ annihilation model looks significantly shallower ($\mathrm{FWHM}_{\min} \propto (L_p^{(\nu\bar{\nu})})^{-1/2}$) than the data, whereas the BZ slope is $\mathrm{FWHM}_{\min} \propto (L_p^{(\mathrm{BZ})})^{-1}$.

The relations found for a common sample of GRBs and blazars by Wu et al. (2016), $\mathrm{MVT} \propto \Gamma_0^{-4.7\pm0.3}$ and $\mathrm{MVT} \propto L_p^{-1.0\pm0.1}$ are both compatible with our samples, although the large scatter observed in our MVT–Γ_0 sample makes it noncritical.

A hyperaccreting Kerr BH with a magnetised torus is expected to power, via BZ, a magnetically dominated jet. MHD simulations identify the BH spin as the main driver of the GRB variability along with the magnetic field strength, although other factors should be considered that contribute to the conversion efficiency of the dissipation of energy into γ-rays (e.g. Granot et al. 2015). The MVT, in terms of minimum duration of pulses, would reflect the timescale of the fastest growing mode of magneto-rotational instabilities in the accretion disc (Janiuk et al. 2021). In this scenario, a higher BH spin would launch a jet with a correspondingly higher Lorentz factor and shorter MVT, thus accounting for the observed correlation. On average, for small values of θ_{obs}, a higher Γ_0 is also expected, although the relation does not always appear to be monotonic for different values of BH spin parameter and magnetic field strength.

6. Conclusions

We proposed a simple definition of MVT of GRB prompt emission as the FWHM of the shortest pulse that is identified through MEPSA, a thoroughly tested GRB peak search algorithm. We applied this method to two independent and complementary GRB data sets: *Swift*/BAT and Insight-HXMT/HE, both of which were split into two groups: Type-I and Type-II GRBs, the former including SEE-GRBs. Firstly, ms-long MVT is very rarely observed, the shortest values being around 10 ms. However, this could be partly due to a S/N-related selection effect. Although the two groups have overlapping MVT distributions, MVT of Type-I GRBs is in the range 10 ms−1 s and is on average significantly shorter than that of Type-II GRBs, which encompasses the range of ∼0.1−100 s. Remarkably, SEE-GRBs with $T_{90} > 2$ s, characterised by deceptively long and structured time profiles such as 060614 and 211211A, also display a short MVT that is more typical of Type-I GRBs, thus propelling this definition of MVT as a useful indicator of the progenitor class, especially in the presence of ambiguous γ-ray time profiles. The origin of this difference could stem from the different ejecta masses that the relativistic jets of either class have to pierce.

Concerning the subsample of Type-II GRBs with measured redshift, upon careful evaluation of the selection effects that impact the MVT measure in the MVT-peak rate plane, we confirm the existence of anti-correlations between MVT and peak luminosity, L_p, and between MVT and initial Lorentz factor of the ejecta Γ_0. Moreover, we were able to establish that MVT also correlates with the number of peaks and the jet opening angle (measured from the achromatic break in the afterglow light curves), although the latter is probably more of a sum of jet and observer angles. Taken together, we find that GRBs with short MVTs (0.1−1 s) on average have narrower jets and/or smaller observer angles ($\lesssim$2−4°), higher Lorentz factors ($\Gamma_0 \gtrsim 100$), high peak luminosities ($L_p \gtrsim 10^{51}$ erg s^{-1}), and exhibit several pulses. A possible interpretation that builds on 3D GRMHD state-of-the-art simulations of a jet propagating through stellar envelopes involves a structured jet with a flat core ($0 \leq \theta < \theta_j$) and a power-law profile that models the jet-cocoon interface ($\theta_j < \theta < \theta_c$). GRBs with short MVTs would be seen within the jet core, resulting in higher L_p and Γ_0, shorter and more numerous peaks, and revealing the true variability imprinted by the inner engine, such as a hyperaccreting BH possibly powered via the Blandford-Znajek mechanism. Conversely, GRBs viewed across the boundary between the jet core and the jet-cocoon interface would appear as less luminous, with lower Lorentz factors and longer MVT due to a smaller Doppler boosting and longer arrival time delays. The possibility that such a jet could wobble randomly within angles comparable to, if not greater than, the jet core itself, further suggests that the different number of peaks observed in different GRBs could indicate how often the jet core points to the observer, thus revealing to what extent the line of sight is off-axis with respect to the average jet direction.

Acknowledgements. We are grateful to the Referee for their useful comments which helped us to improve the paper. A.E.C. and C.G. acknowledge financial support from FIRD 2022 of UNIFE Dept. Physics and Earth Science under the project "Caratterizzazione e simulazioni di curve di luce di Gamma-Ray Burst come processi stocastici e validazione attraverso tecniche di machine learning" (PI: CG). C.G.M. and N.J.M. acknowledge support from Hiroko and Jim Sherwin. This work is supported by the National Program on Key Research and Development Project (2021YFA0718500) and the National Natural Science Foundation of China under grants 11733009, U1838201 and U1838202. This work made use of data from the Insight-HXMT mission, a project funded by China National Space Administration (CNSA) and the Chinese Academy of Sciences (CAS).

References

Abbasi, R., Ackermann, M., Adams, J., et al. 2022, ApJ, 939, 116
Ahumada, T., Singer, L. P., Anand, S., et al. 2021, Nat. Astron., 5, 917
Amati, L. 2021, Nat. Astron., 5, 877
Barthelmy, S. D., Barbier, L. M., Cummings, J. R., et al. 2005, Space Sci. Rev., 120, 143
Bhat, P. N. 2013, ArXiv e-prints [arXiv:1307.7618]
Bhat, P. N., Briggs, M. S., Connaughton, V., et al. 2012, ApJ, 744, 141
Bishop, C. M. 2006, Pattern Recognition and Machine Learning (Information Science and Statistics) (Berlin, Heidelberg: Springer-Verlag)
Blandford, R. D., & Znajek, R. L. 1977, MNRAS, 179, 433
Borgonovo, L., Frontera, F., Guidorzi, C., et al. 2007, A&A, 465, 765
Bromberg, O., Nakar, E., Piran, T., & Sari, R. 2013, ApJ, 764, 179
Bucciantini, N., Metzger, B. D., Thompson, T. A., & Quataert, E. 2012, MNRAS, 419, 1537
Budai, A., Raffai, P., Borgulya, B., et al. 2020, MNRAS, 491, 1391
Bustamante, M., Baerwald, P., Murase, K., & Winter, W. 2015, Nat. Commun., 6, 6783
Bustamante, M., Heinze, J., Murase, K., & Winter, W. 2017, ApJ, 837, 33
Cao, X., Jiang, W., Meng, B., et al. 2020, Sci. China-Phys. Mech. Astron., 63, 249504
Chen, Y., Cui, W., Li, W., et al. 2020, Sci. China-Phys. Mech. Astron., 63, 249505
Dado, S., & Dar, A. 2022, ApJ, 940, L4
D'Avanzo, P., Salvaterra, R., Bernardini, M. G., et al. 2014, MNRAS, 442, 2342
De Colle, F., Ramirez-Ruiz, E., Granot, J., & Lopez-Camara, D. 2012, ApJ, 751, 57
Della Valle, M., Chincarini, G., Panagia, N., et al. 2006, Nature, 444, 1050
Dichiara, S., Guidorzi, C., Amati, L., Frontera, F., & Margutti, R. 2016, A&A, 589, A97
Dichiara, S., Gropp, J. D., Kennea, J. A., et al. 2022, ATel, 15650, 1
Eichler, D., Livio, M., Piran, T., & Schramm, D. N. 1989, Nature, 340, 126
Fargion, D. 2001, ArXiv e-prints [arXiv:astro-ph/0104446]
Fenimore, E. E., & Ramirez-Ruiz, E. 2000, ArXiv e-prints [arXiv:astro-ph/0004176]
Fenimore, E. E., in 't Zand, J. J. M., Norris, J. P., Bonnell, J. T., & Nemiroff, R. J. 1995, ApJ, 448, L101
Fermi-LAT Collaboration 2021, Nat. Astron., 5, 385
Fong, W.-F., Nugent, A. E., Dong, Y., et al. 2022, ApJ, 940, 28
Frederiks, D., Lysenko, A., Ridnaia, A., et al. 2022, GRB Coordinates Network, 32668, 1

Fynbo, J. P. U., Watson, D., Thöne, C. C., et al. 2006, Nature, 444, 1047
Gao, H., Lei, W.-H., & Zhu, Z.-P. 2022, ApJ, 934, L12
Ge, M. Y., Chen, Y. P., Liao, J. Y., et al. 2022, ATel, 15703, 1
Gehrels, N. 1986, ApJ, 303, 336
Gehrels, N., Chincarini, G., Giommi, P., et al. 2004, ApJ, 611, 1005
Gehrels, N., Norris, J. P., Barthelmy, S. D., et al. 2006, Nature, 444, 1044
Ghirlanda, G., Nappo, F., Ghisellini, G., et al. 2018, A&A, 609, A112
Golkhou, V. Z., & Butler, N. R. 2014, ApJ, 787, 90
Golkhou, V. Z., Butler, N. R., & Littlejohns, O. M. 2015, ApJ, 811, 93
Gomboc, A., Kobayashi, S., Guidorzi, C., et al. 2008, ApJ, 687, 443
Gompertz, B. P., Ravasio, M. E., Nicholl, M., et al. 2023, Nat. Astron., 7, 67
Gottlieb, O., Levinson, A., & Nakar, E. 2019, MNRAS, 488, 1416
Gottlieb, O., Levinson, A., & Nakar, E. 2020a, MNRAS, 495, 570
Gottlieb, O., Bromberg, O., Singh, C. B., & Nakar, E. 2020b, MNRAS, 498, 3320
Gottlieb, O., Nakar, E., & Bromberg, O. 2021a, MNRAS, 500, 3511
Gottlieb, O., Bromberg, O., Levinson, A., & Nakar, E. 2021b, MNRAS, 504, 3947
Gottlieb, O., Liska, M., Tchekhovskoy, A., et al. 2022a, ApJ, 933, L9
Gottlieb, O., Moseley, S., Ramirez-Aguilar, T., et al. 2022b, ApJ, 933, L2
Gottlieb, O., Lalakos, A., Bromberg, O., Liska, M., & Tchekhovskoy, A. 2022c, MNRAS, 510, 4962
Granot, J., Piran, T., Bromberg, O., Racusin, J. L., & Daigne, F. 2015, Space Sci. Rev., 191, 471
Guidorzi, C. 2015, Astron. Comput., 10, 54
Guidorzi, C., Frontera, F., Montanari, E., et al. 2005, MNRAS, 363, 315
Guidorzi, C., Frontera, F., Montanari, E., et al. 2006, MNRAS, 371, 843
Guidorzi, C., Dichiara, S., & Amati, L. 2016, A&A, 589, A98
Hascoët, R., Daigne, F., Mochkovitch, R., & Vennin, V. 2012, MNRAS, 421, 525
Janiuk, A., James, B., & Palit, I. 2021, ApJ, 917, 102
Japelj, J., Kopač, D., Kobayashi, S., et al. 2014, ApJ, 785, 84
Jin, Z.-P., Li, X., Cano, Z., et al. 2015, ApJ, 811, L22
Jordana-Mitjans, N., Mundell, C. G., Guidorzi, C., et al. 2022, ApJ, 939, 106
Kann, D. A., Klose, S., Zhang, B., et al. 2011, ApJ, 734, 96
Kobayashi, S., Piran, T., & Sari, R. 1997, ApJ, 490, 92
Kobayashi, S., Ryde, F., & MacFadyen, A. 2002, ApJ, 577, 302
Kocevski, D., & Petrosian, V. 2013, ApJ, 765, 116
Kouveliotou, C., Meegan, C. A., Fishman, G. J., et al. 1993, ApJ, 413, L101
Kozyrev, A. S., Golovin, D. V., Litvak, M. L., et al. 2022, GRB Coordinates Network, 32805, 1
Kumar, P., & Panaitescu, A. 2008, MNRAS, 391, L19
Kumar, P., McMahon, E., Panaitescu, A., et al. 2007, MNRAS, 376, L57
Lazzati, D., & Begelman, M. C. 2006, ApJ, 641, 972
Lei, W. H., Wang, D. X., Gong, B. P., & Huang, C. Y. 2007, A&A, 468, 563
Li, T.-P. 2001, Chin. J. Astron. Astrophys., 1, 313
Li, T.-P. 2007, Nucl. Phys. B Proc. Suppl., 166, 131
Liang, E.-W., Lin, T.-T., Lü, J., et al. 2015, ApJ, 813, 116
Lien, A., Sakamoto, T., Barthelmy, S. D., et al. 2016, ApJ, 829, 7
Littlejohns, O. M., & Butler, N. R. 2014, MNRAS, 444, 3948
Liu, C. Z., Zhang, Y. F., Li, X. F., et al. 2020, Sci. China-Phys. Mech. Astron., 63, 249503
Lü, J., Zou, Y.-C., Lei, W.-H., et al. 2012, ApJ, 751, 49
Lyutikov, M. 2006, MNRAS, 369, L5
Lyutikov, M., & Blandford, R. 2003, ArXiv e-prints [arXiv:astro-ph/0312347]
MacFadyen, A. I., & Woosley, S. E. 1999, ApJ, 524, 262
MacLachlan, G. A., Shenoy, A., Sonbas, E., et al. 2012, MNRAS, 425, L32
MacLachlan, G. A., Shenoy, A., Sonbas, E., et al. 2013, MNRAS, 432, 857
MAGIC Collaboration (Acciari, V. A., et al.) 2019, Nature, 575, 455
Margutti, R. 2009, Toward New Insights on the Gamma-ray Burst Physics: From X-ray Spectroscopy to the Identification of Characteristic Time Scales (Milan: Università degli Studi Milano-Bicocca)
Margutti, R., Guidorzi, C., Chincarini, G., et al. 2008, in 2008 Nanjing Gamma-ray Burst Conference, eds. Y. F. Huang, Z. G. Dai, & B. Zhang, AIP Conf. Ser., 1065, 259
Margutti, R., Guidorzi, C., & Chincarini, G. 2011, Int. J. Mod. Phys. D, 20, 1969
Metzger, B. D., Quataert, E., & Thompson, T. A. 2008, MNRAS, 385, 1455
Molinari, E., Vergani, S. D., Malesani, D., et al. 2007, A&A, 469, L13
Mundell, C. G., Kopac, D., Arnold, D. M., et al. 2013, Nature, 504, 119
Narayan, R., Paczynski, B., & Piran, T. 1992, ApJ, 395, L83
Nava, L., Sironi, L., Ghisellini, G., Celotti, A., & Ghirlanda, G. 2013, MNRAS, 433, 2107
Norris, J. P., & Bonnell, J. T. 2006, ApJ, 643, 266
Norris, J. P., Nemiroff, R. J., Bonnell, J. T., et al. 1996, ApJ, 459, 393
Nugent, A. E., Fong, W.-F., Dong, Y., et al. 2022, ApJ, 940, 23
Paczynski, B. 1991, Acta Astron., 41, 257
Paczyński, B. 1998, ApJ, 494, L45
Planck Collaboration VI. 2020, A&A, 641, A6
Popham, R., Woosley, S. E., & Fryer, C. 1999, ApJ, 518, 356
Portegies Zwart, S. F., & Totani, T. 2001, MNRAS, 328, 951
Portegies Zwart, S. F., Lee, C.-H., & Lee, H. K. 1999, ApJ, 520, 666
Press, W. H., Teukolsky, S. A., Vetterling, W. T., & Flannery, B. P. 1992, Numerical Recipes in C. The Art of Scientific Computing (Cambridge: Cambridge University Press)
Racusin, J. L., Karpov, S. V., Sokolowski, M., et al. 2008, Nature, 455, 183
Rastinejad, J. C., Gompertz, B. P., Levan, A. J., et al. 2022, Nature, 612, 223
Reichart, D. E., Lamb, D. Q., Fenimore, E. E., et al. 2001, ApJ, 552, 57
Reynoso, M. M., Romero, G. E., & Sampayo, O. A. 2006, A&A, 454, 11
Roberts, O. J., Veres, P., Baring, M. G., et al. 2021, Nature, 589, 207
Rossi, A., Rothberg, B., Palazzi, E., et al. 2022, ApJ, 932, 1
Salafia, O. S., Ghisellini, G., Pescalli, A., Ghirlanda, G., & Nappo, F. 2016, MNRAS, 461, 3607
Salafia, O. S., Barbieri, C., Ascenzi, S., & Toffano, M. 2020, A&A, 636, A105
Sari, R., & Piran, T. 1999, ApJ, 520, 641
Sonbas, E., MacLachlan, G. A., Dhuga, K. S., et al. 2015, ApJ, 805, 86
Song, X.-Y., Xiong, S.-L., Zhang, S.-N., et al. 2022, ApJS, 259, 46
Steele, I. A., Kopač, D., Arnold, D. M., et al. 2017, ApJ, 843, 143
Svinkin, D., Frederiks, D., Hurley, K., et al. 2021, Nature, 589, 211
Troja, E., Fryer, C. L., O'Connor, B., et al. 2022, Nature, 612, 228
Tsvetkova, A., Frederiks, D., Golenetskii, S., et al. 2017, ApJ, 850, 161
van Eerten, H. J., & MacFadyen, A. I. 2012, ApJ, 751, 155
van Eerten, H., Zhang, W., & MacFadyen, A. 2010, ApJ, 722, 235
Vianello, G., Gill, R., Granot, J., et al. 2018, ApJ, 864, 163
Woosley, S. E. 1993, ApJ, 405, 273
Wu, Q., Zhang, B., Lei, W.-H., et al. 2016, MNRAS, 455, L1
Wu, B., Zhang, Y., Li, X., et al. 2022, Exp. Astron., 53, 1037
Xiao, S., Xiong, S. L., Liu, C. Z., et al. 2020, J. High Energy Astrophys., 26, 58
Xiao, S., Zhang, Y. Q., Zhu, Z. P., et al. 2022, ArXiv e-prints [arXiv:2205.02186]
Xie, W., Lei, W.-H., & Wang, D.-X. 2017, ApJ, 838, 143
Xie, L., Wang, X.-G., Zheng, W., et al. 2020, ApJ, 896, 4
Xin, L.-P., Wang, Y.-Z., Lin, T.-T., et al. 2016, ApJ, 817, 152
Xue, L., Zhang, F.-W., & Zhu, S.-Y. 2019, ApJ, 876, 77
Yang, J., Chand, V., Zhang, B.-B., et al. 2020, ApJ, 899, 106
Yang, J., Ai, S., Zhang, B. B., et al. 2022, Nature, 612, 232
Yi, S.-X., Lei, W.-H., Zhang, B., et al. 2017, J. High Energy Astrophys., 13, 1
Zhang, B. 2006, Nature, 444, 1010
Zhang, B., & Mészáros, P. 2004, Int. J. Mod. Phys. A, 19, 2385
Zhang, B., & Yan, H. 2011, ApJ, 726, 90
Zhang, B., Zhang, B.-B., Liang, E.-W., et al. 2007, ApJ, 655, L25
Zhang, S.-N., Li, T., Lu, F., et al. 2020, Sci. China Phys. Mech. Astron., 63, 249502
Zhang, B. B., Liu, Z. K., Peng, Z. K., et al. 2021, Nat. Astron., 5, 911
Zhao, W., Zhang, J.-C., Zhang, Q.-X., et al. 2020, ApJ, 900, 112

Appendix A: Estimating the peak FWHM through MEPSA

The Multiple Excess Peak Search Algorithm (MEPSA) is an algorithm aimed at identifying peaks in LCs affected by uncorrelated Gaussian noise. MEPSA scans the time series at different timescales by comparing a peak candidate with a variable number of adjacent bins; the number of adjacent bins involved in the detection is called $N_{\rm adiac}$.

When the entire LC has been screened, the process is re-run on the rebinned versions of the same curve; each time the rebinning factor is increased by one up to a maximum established by the user. At the end of the procedure, MEPSA provides the detection timescale $\Delta t_{\rm det}$ for each peak candidate; this is the product between the original time resolution of the time series and the rebinning factor. We refer the reader to Guidorzi (2015) for a more detailed description.

Since MEPSA does not provide direct information on the FWHM of a detected peak, we had to preliminarily calibrate it, starting from the rule of thumb declared in Guidorzi (2015). This establishes a set of different scalings between $\Delta t_{\rm det}$ and FWHM for different ranges of S/N. In order to determine a more precise calibration between the FWHM, $\Delta t_{\rm det}$, and S/N, we simulated LCs with FWHM values taken from a given lognormal distribution. For our calibration, we used 1600 fast rise and exponential decay (FRED) profiles:

$$F(t) = \begin{cases} A \exp\left[-\left(\frac{t_0 - t}{t_r}\right)^p \right], & \text{if } t < t_0 \\ A \exp\left[-\left(\frac{t - t_0}{t_d}\right)^p \right], & \text{if } t \geq t_0 \end{cases}, \tag{A.1}$$

with $t_0 = 0$, $p = 1.5$; $t_d = 3t_r$; and FWHM $= 10^x$ s, where x is the random normal distributed with $\mu = \log 0.6$ and $\sigma = 0.5$, following the same prescriptions adopted in Guidorzi (2015). Simulated LCs at 1 ms were rebinned with rebinning factors = 1, 4, 64, and 1000. These profiles were affected by uncorrelated Gaussian noise.

We tried to include more parameters provided by MEPSA to see whether we could further reduce the scatter around the best fitting relation. To this aim, we assumed that the FWHM could be described by the following relation:

$$\mathrm{FWHM} \propto \Delta t_{\rm det} \left(\frac{\mathrm{S/N}}{\mathrm{S/N_0}} - 1 \right)^{\alpha} \mathrm{P}^{\beta}, \tag{A.2}$$

where $\mathrm{S/N_0}$ is a hard lower limit for S/N that had preliminarily been fixed to 4.7, P is a generic MEPSA parameter and α and β are power-law indices to be determined. After choosing P, we considered the corresponding logarithmic quantities of the multiplicative terms in Eq. (A.2) and determined α and β by finding the maximum likelihood within a linear model regression approach (see Section 3.1.1 of Bishop 2006). As a result, we found a significant improvement by using $N_{\rm adiac}$ as the third parameter P. As shown in Figure A.1, the best fitting relation correlates FWHM with $\Delta t_{\rm det}$, the S/N, and $N_{\rm adiac}$:

$$\mathrm{FWHM} = 10^{-0.31}\, \Delta t_{\rm det} \left(\frac{\mathrm{S/N}}{4.7} - 1 \right)^{0.60} \mathrm{N}_{\rm adiac}^{1.06}. \tag{A.3}$$

$$\sigma_{\rm FWHM} = \mathrm{FWHM}\, (10^{\pm 0.13} - 1)$$

The scatter around the best fitting relation, expressed by $\sigma_{\rm FWHM}$, is calculated as the multiplicative coefficient that corresponds to the logarithmic standard deviation of the simulated points. To account for the asymmetric nature of the corresponding uncertainty on the FWHM, in Eq. (A.3) we distinguish between negative and positive uncertainties, but in practice the $1-\sigma$ uncertainty on the FWHM that affects the calibration of Eq. A.3 is about 35%. Consequently, all the FWHM values and relative uncertainties that were derived through MEPSA in this paper were calculated using Eq. (A.3).

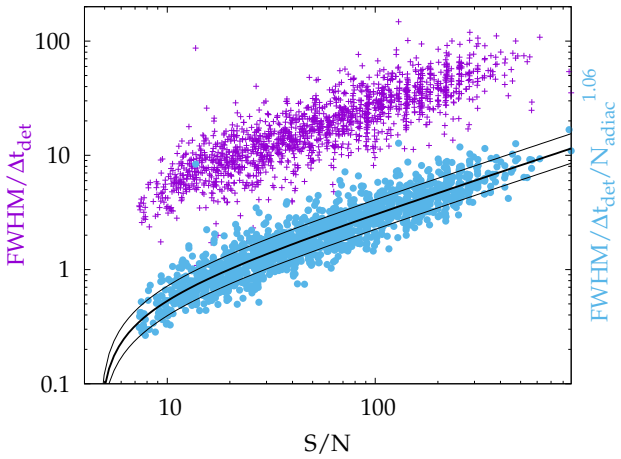

Fig. A.1. Ratio between true FWHM and MEPSA detection timescale $\Delta t_{\rm det}$ (red crosses; left-hand side vertical axis) versus S/N for a sample of simulated GRB-like pulses. The right vertical axis displays the same ratio further divided by MEPSA parameter $N_{\rm adiac}^{1.06}$ for the same data set (blue circles). The latter quantity is found to minimise the scatter around the best fitting relation.